

General Disclaimer

One or more of the Following Statements may affect this Document

- This document has been reproduced from the best copy furnished by the organizational source. It is being released in the interest of making available as much information as possible.
- This document may contain data, which exceeds the sheet parameters. It was furnished in this condition by the organizational source and is the best copy available.
- This document may contain tone-on-tone or color graphs, charts and/or pictures, which have been reproduced in black and white.
- This document is paginated as submitted by the original source.
- Portions of this document are not fully legible due to the historical nature of some of the material. However, it is the best reproduction available from the original submission.

(NASA-CR-170976) DOPPLER LIDAR SIGNAL AND
TURBULENCE STUDY Final Report (FWG)
Associates, Inc.) 58 p HC A04/MF A01

N84-17574

CSCL 20E G3

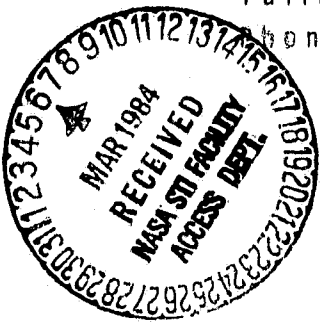
Unclassified
00528

36

FWG

FWG ASSOCIATES, INC.

R. R. 2, Box 271-A
Tullahoma, TN 37388
Phone: 615/455-1982



Prepared by:

Walter Frost
K. H. Huang

Prepared for:

NASA
Marshall Space Flight Center, AL 35812
Attn: Dr. Dan Fitzjarrald/ED42

FINAL REPORT

Contract NAS8-35185

DOPPLER LIDAR SIGNAL AND
TURBULENCE STUDY

December 23, 1983

Approved:



Dr. Walter Frost, President

ABSTRACT

Wind fields were measured with the ground-based NASA/MSFC lidar and with the NASA RB-57 instrumented aircraft. The remotely sensed winds are compared with the in situ aircraft measurements. The mean wind fields, the turbulence intensities, and the turbulence spectra determined from measurements by both systems are in very good agreement. Turbulence intensities and spectra were calculated from the fluctuations with time in the radial wind speed component. It should be noted that time histories of the radial wind represent values spatially averaged over a 300-m volume element. The lidar winds were sampled at approximately 2 times per second whereas the aircraft measurements were sampled at 40 times per second.

The second moment or Doppler frequency spectral width of the lidar measurements was also compared with turbulence intensities measured by the aircraft. These second moments could only be resolved at the very low altitudes (in three range bins). Turbulence intensities estimated from the spectral width data were an order of magnitude higher than that measured by the aircraft.

An interesting boundary layer evolved during the progress of the experiment. The breakup of a stable boundary layer resulted in winds blowing in one direction above 600 m ms⁻¹ and in the opposite direction below that level. Both the aircraft and the lidar systems clearly identified this unusual boundary layer flow and showed the identical trends. The clear identification of the unusual boundary layer by both systems further augment the reliability of the remotely measured wind speeds and turbulence.

ACKNOWLEDGMENT

This research was supported under NASA Contract NAS8-35185. The authors are grateful for funding from the Office of Aeronautical and Space Technology, NASA Headquarters, Washington, D.C. The support of A. Richard Tobiason and Dennis W. Camp is acknowledged. Special thanks go to Dan Fitzjarrald of the System Dynamics Laboratory, Atmospheric Sciences Division, NASA/George C. Marshall Space Flight Center, Huntsville, Alabama, who monitored the research program.

TABLE OF CONTENTS

SECTION	PAGE
1.0 INTRODUCTION	1
2.0 INSTRUMENTATION AND DATA	3
2.1 Lidar	3
2.2 Aircraft	4
3.0 COMPARISON OF LIDAR MEASUREMENTS WITH AIRCRAFT MEASUREMENTS . .	7
3.1 Mean Wind	7
3.2 Turbulence	8
4.0 CONCLUSIONS	12
REFERENCES CITED	13

1.0 INTRODUCTION

A field test was carried out to compare lidar-measured winds and turbulence with both aircraft measurements and tower array measurements. The instrumentation consisted of the NASA/MSFC lidar (Bilbro and Vaughan 1978), the NASA RB-57 instrumented aircraft (Camp et al. 1983), and the NASA/MSFC Atmospheric Boundary Layer Facility eight-tower array (Frost and Lin 1983). The experiment called for three days of testing.

On May 10, 1983, the Doppler lidar was set in a conical scanning mode. Scans were carried out at vertical angles of 6° , 19° , 26° , and 32° . The aircraft then flew circular flight paths at increasingly higher altitudes in order to approximately capture the lidar beam as illustrated in Figure 1. On May 11 the lidar was down for repairs and adjustments and only flights over the tower array were carried out. On May 12 the lidar was fixed at a 6° vertical angle and at 52° azimuthal from true north, see Figure 2. The aircraft then flew approach paths at an approximate 4° glide slope parallel to the radar beam. Eight successive runs or approach paths were flown at approximately 5-minute intervals. On all three days, May 10-12, the tower array was operated. The aircraft made several passes directly over the towers to provide data for comparing flight measurements with ground-based tower measurements. These data, however, are not analyzed to any extent in this report.

The emphasis of the study was to compare Doppler-lidar-measured winds and turbulence with aircraft measurements. Primarily the study was to compare aircraft-measured turbulence intensities with the lidar

second moment or spectral width data. Unfortunately, this aspect of the study was not particularly successful in view of the fact that only three range bins (Range Bin 9, 10, and 11) had high enough signal-to-noise ratio for the second moments to be successfully computed.

Secondly, the values computed in the range from 1.26 to 2.51 m/s, which is a factor of ten larger than those values measured either with the aircraft or with the tower array.

The field study was successful, however, in that it: (1) provided a unique set of data for comparing mean wind speed values; (2) revealed that turbulence intensities computed from the Doppler-measured wind speed time histories (i.e., 300 m spatially averaged values) agree remarkably well with the point measurement from the aircraft; and (3) showed that turbulence spectra calculated both from the time histories of the lidar-measured winds and the aircraft-measured winds were in very good agreement.

Finally, an extremely interesting atmospheric boundary layer event evolved during the time period (16:42-17:78 zulu) of the May 12, 1983, test. This event was clearly recorded by both the aircraft instrumentation and the lidar. Because both systems accurately recorded this boundary layer event, it is believed that considerable reliability in the lidar mean winds is demonstrated.

This report presents a detailed analysis of the winds measured during the evolution of the atmospheric boundary layer occurring on May 12, 1983, and emphasizes the validation of the Doppler lidar remote measurements with the in situ aircraft measurements.

2.0 INSTRUMENTATION AND DATA

2.1 Lidar

A complete description of the NASA/MSFC Doppler lidar is provided in Bilbro and Vaughan (1978), Jeffreys and Bilbro (1975), and Lee (1982). The lidar is a variably pulsed CO₂ Doppler lidar. During this study, a 2-μs-pulsed lidar was used. The Doppler measures the component of the wind along the lidar beam, i.e., the radial wind speed component. The measurements are representative of the average wind speed within a conical trapezoid of 300 m in length and of diameter associated with the diverging lidar beam width. Figure 2 illustrates the lidar beam and shows the location of each individual range bin for which radial wind speed components are measured. The figure also illustrates the position of the beam relative to the terrain contour cross section.

The lidar data were received from NASA/MSFC in digitized format on magnetic tapes. The data format for a given tape is shown in Table 1. Data for roughly 189 range bins is calculated every half second, as illustrated in the table. Typical time histories of the data provided on the tape, which includes amplitude of the signal in decibels, radial wind velocity in meters per second (m/s), and second moment (lidar width) data for turbulence intensities in meters per second, are shown in Figure 3 for the May 10 and 12 field tests, respectively. The lidar width data is recorded as an integer index. The corresponding value of each integer index is given in Table 2.

Figure 4 is a plot of 150 sequential values of wind velocity from the May 12, 1983, data tape. The figure illustrates approximately 75

seconds of data. It is clear from the figure that data in Range Bins 1 through 8 are very noisy due to ground clutter and do not provide useful data. Also, the figure shows that beyond approximately Range Bin 21 the signal-to-noise ratio becomes excessive and velocities measured above this altitude are not meaningful. Thus for the May 12 field test, only radial wind speed values from Range Bin 9 (460 m ms1) to Range Bin 21 (840 m ms1) were selected for analysis.

2.2 Aircraft

Data from the RB-57 flights consisted of 80 variables in a 60-bit integer format. The original raw data were sampled at 200 cycles per second. However, they were provided from NASA/Langley in engineering units at 40 samples per second. Although all the variables necessary to resolve the wind speed components by backing out the aircraft motion are available, the data from Langley provided pre-computed gust velocities. These were used throughout the analysis. Table 3 provides a sample of the aircraft data.

Data sets for eight flights along an approximate 4° glide slope parallel to the lidar beam were collected. Additionally, four level flights perpendicular and parallel to the tower array were made and data provided. The tower data, however, are not analyzed to any extent in this report. Figure 2 shows typical flight paths relative to the lidar beam. Because of unusual drift in the INS, the latitude and longitude measurements are questionable. Thus the exact position of the aircraft relative to the lidar beam in a horizontal plane is not known. Ground-based personnel, however, observed the aircraft to approach essentially

along the lidar beam. Moreover, the aircraft height at any instant is accurately measured and is, in fact, the most important value of aircraft position for comparing the wind speeds measured by the two systems.

The horizontal wind measured by the aircraft in terms of wind speed, magnitude, and direction are plotted in Figure 5 for all eight runs. One observes that during the May 12 field test a strong inversion developed at approximately 600 m above the elevation of the lidar site. This resulted in decoupling of the wind with the wind blowing in one direction aloft and another direction at the surface; along some flight paths, the wind is observed to change direction by as much as 180°.

Figure 6 is a three-dimensional plot of the horizontal winds measured with the aircraft along each flight path and staggered in time. In this plot the wind vectors illustrated are values averaged over a 300 m section along the flight path. One observes the growth of the inversion layer over the 30-minute period during which the eight flights were carried out.

The temperature variation with height along the flight path was computed and is plotted in Figure 7. It is apparent from the data that although the temperature gradient aloft represents a heat flux toward the surface of the earth, the potential gradient is, in general, positive. Values of the gradient and flux Richardson's number, respectively, were computed based on parameters averaged along the entire flight path. The results were not meaningful in that the flux Richardson number was a relatively large negative value while the gradient Richardson number was positive and on the order of 0.25, which represents an extremely stable boundary layer.

In order to attempt to resolve this anomaly, the velocity profile was broken up into multiple sections as illustrated in Figure 8. A linear curve was fit to each segment of the velocity profile and the slope (i.e., velocity gradient) for that segment computed. The values of the curve fit parameters are tabulated in Figure 8. The Richardson number was then plotted for the individual sections of the atmosphere. These results are plotted in Figures 9 and 10. The meaning of the results, however, is not clear in terms of the classical Richardson number for flow over flat terrain. (Note, however, that the terrain is not flat since Mankin Mountain (approximately 350 m msl) is directly under the flight path.)

Inspection of the first plot of Figure 9 is obviously not meaningful. The next two plots show unacceptably large values of Ri below 450 m msl but neutral or slightly unstable flow aloft. The latter plots illustrate that the lower layer has become unstable (undoubtedly due to heating from the ground) and that the neutral layer is growing downward. The flux Richardson number given in Figure 10 shows even less decisive results. The reliability of the Richardson number prediction is obviously, at most, marginal.

Further analysis of the data, including the results from the tower measurements, will be carried out under subsequent efforts to attempt to provide a better physical explanation of the mechanism generating the observed boundary layer behavior.

3.0 COMPARISON OF LIDAR MEASUREMENTS WITH AIRCRAFT MEASUREMENTS

3.1 Mean Wind

Comparison of the measurements of mean wind with the lidar and with the aircraft system is described in this section. The aircraft-measured wind speeds were first transformed to the time-dependent components along a 6° line of sight and at 52° azimuthal true north, i.e., along the lidar beam.

The aircraft-measured wind speeds were then averaged with time over a period corresponding to the length of time required for the aircraft to traverse the 300-m range bins along the flight path. Two approaches to carrying out this averaging technique were investigated. One was to assume vertical homogeneity in the flow field. The averaging process for the aircraft data was then carried out as illustrated in Figure 11(a). The alternate technique was to average the wind assuming homogeneity in the horizontal direction. This approach is illustrated in Figure 11(b).

A third effect taken into account when comparing data from the two systems was to assure that the winds measured with lidar and with the aircraft were measured in the same time period. The run times associated with each flight path were therefore overlaid on the lidar-measured winds as illustrated in Figure 12. The lidar data are sampled in each bin at approximately 0.5-second intervals. The segment of the lidar wind speed time history associated with the time period in which the aircraft was passing through or parallel to that range bin was then averaged.

Figures 13 and 14 compare the lidar-measured winds averaged over the time period, as described above, with the aircraft-measured winds averaged over the corresponding 300-m section assuming vertical homogeneity and horizontal homogeneity, respectively. One observes very good agreement between the lidar measurements and aircraft measurements although the data is consistently higher for the lidar measurements. Although the exact cause of this difference is not known, it is reasonable to assume that due to the unusual drift in the INS the aircraft velocity may be low because of the Schuler oscillation phenomenon.

In general, the trends of the aircraft-measured wind most closely follow the lidar measurements when the assumption of vertical homogeneity is made. This implies that the best agreement is achieved when the aircraft is at the same distance from the lidar even though it may be above or below the lidar beam at that distance. Horizontal homogeneity, of course, implies that the aircraft is making measurements at the same height as the lidar beam for the given range bin but may be further or closer to the lidar location in horizontal distance. It should be noted that no attempt is made to correct the velocities for convective effects, i.e., translation of the air parcel parallel to the lidar beam, nor for surface terrain contour effects. A terrain correction may help improve the data comparison since the lidar beam passed directly over the top of a mountain, whereas some of the flight paths may have passed to one side or the other. The agreement of the data is believed to be sufficiently good; thus, no terrain correction was attempted.

3.2 Turbulence

Computed turbulence intensities for the radial wind speed component from the aircraft measurements and the lidar measurements are also shown in Figures 13 and 14. In these figures the turbulence intensity of the lidar-measured wind is computed from

$$\sigma_w = \frac{1}{N} \sqrt{\sum_{n=1}^N (W(t) - \bar{W})^2}$$

where \bar{W} is the average wind speed for the period of time the aircraft passes through or parallel to the range bin of interest and $W(t)$ is the fluctuation in wind. The summation is carried out over N time increments of $\Delta t = 0.455$ second which lapses the time interval between the aircraft entering and leaving the range bin. This time interval is used both in computing the aircraft turbulence intensity, illustrated in the figure by the small plus signs, and the lidar turbulence intensity, indicated by the small circles. The interesting result is that the turbulence intensities, although scattered, are intermingled, indicating general agreement between the lidar-measured turbulence intensity and the aircraft-measured values. This is particularly true for the lower range bins.

This result is an important observation. It is apparent that results from the present study contradict this thinking. It is generally thought that the Doppler second moment data will correlate with essentially point measured turbulence intensities obtained from the aircraft. The fluctuations in the radial wind component time history, on the other hand, being values of wind averaged over the spatial extent of the range bin, are thought not to necessarily

correspond to turbulence measured internal to the volume element.

As noted earlier, only three range bin values of spectral width determined turbulence intensities could be extracted from the lidar signal. These values, converted to meters per second in Table 2, range from 1.26 to 2.51 m/s; almost a factor of ten larger than values measured by the aircraft or computed from the lidar data as described above.

In order to investigate the turbulence measurements further, the turbulent energy spectra were computed. Turbulence spectra were computed for each of the eight flight paths and at each corresponding range bin, assuming vertical homogeneity. The spectrum computed for each range bin for the eight aircraft flights was then segment averaged to provide the spectra illustrated by the small plus signs in Figure 15. Similarly, spectra for a 2-minute time period begin at the time the aircraft enters the range bin, or a region parallel to it, were then computed from the lidar data. Note these data are sampled at approximately two times per second resulting in a Nyquist frequency of approximately 1 Hz. The aircraft data, on the other hand, are sampled at 40 times per second resulting in a Nyquist frequency of 20 Hz. The spectra computed from the lidar data were only five segment averaged. The reason for this is illustrated by inspection of Figure 12. At times corresponding to some of the later aircraft flights, the radial wind measured by the lidar at the higher elevations or higher numbered range bins (i.e., approximately Range Bins 16 through 21) were extremely intermittent. This is probably due to cloud formation during the later runs. Therefore, although these time histories provide a reasonably

valid average or mean wind speed, they do not allow a valid spectrum to be computed. At the lower range bins (i.e., Range Bins 11 through 16), very good agreement with the aircraft data is observed. Note Range Bins 9 and 10 were not used because very few aircraft flights descend to that height.

Although the data do not fall on top of one another because of the different sampling frequencies involved, the spectra do merge together forming a relatively continuous line. This indicated that the distribution of turbulent intensity in the frequency domain is essentially the same for both measurements. The disagreement in spectra at the higher range bins is due to increasing noise or decreasing signal-to-noise ratio, which is clearly apparent in Figure 12.

The very good agreement both in turbulence intensity and turbulence spectral properties occurring in the clear-air measurements leads to the conclusion that computed values of turbulence properties using the time history of the lidar-measured winds provide highly meaningful results. Although further research is required, this suggests that the second moment or spectral width of the Doppler frequency from the lidar may not be necessary in order to compute turbulence properties. If this is true, the time history of the wind speeds measured by the lidar can simply be analyzed for turbulent statistical properties of interest.

4.0 CONCLUSIONS

It is concluded that very good agreement between remotely sensed winds using a ground-based Doppler lidar and in situ measurements with an instrumented aircraft is possible. Results show that turbulence intensities computed from time histories measured with the aircraft and time histories of the radial wind measured with lidar can be analyzed statistically to provide turbulence intensities and turbulence spectra which agree well with one another. The results further show that the second moment data, as presently computed with the NASA/MSFC algorithms, do not provide meaningful comparisons with turbulence intensities measured with the aircraft. This disagreement, however, must be investigated further in terms of the accuracy of the second moment data determined by both the lidar hardware and the algorithm for computing the second moment.

Finally, additional insight into making turbulence measurements with lidar can be achieved by analyzing the May 10, 1983, results when the aircraft data is available from NASA/Langley Research Center. Also, an analysis of the signal-to-noise ratio with the object of calibrating the turbulence intensity at higher bin numbers with aircraft data should be carried out. The result would provide a reliable and accurate technique for calibrating the lidar and, thus, of remotely sensing turbulence in the atmosphere.

References Cited

Bilbro, J. W. and W. W. Vaughan (1978): "Wind Field Measurement in the Nonprecipitous Regions Surrounding Severe Storms by an Airborne Pulsed Doppler Lidar System," Bulletin of the Am. Met. Soc., 59(9):1095.

Campbell, W., D. W. Camp, W. Frost (1983): "An Analysis of Spanwise Gust Gradient Data," Preprints: Ninth Conference on Aerospace and Aeronautical Meteorology, June 6-9, 1983, Omaha, Neb. Am. Met. Soc., Boston, Mass.

Frost, W. and M. C. Lin (1983): "Statistical Analysis of Turbulence Data from the NASA Marshall Space Flight Center Atmospheric Boundary Layer Tower Array Facility," Final report under NAS8-34627 prepared for NASA/MSFC, Huntsville, Ala.

Jeffreys, H. B. and J. W. Bilbro (1975): "Development of a Laser Doppler System for the Detection and Monitoring of Atmospheric Disturbances," NASA TM X-64981, NASA/MSFC.

Lee, R. W. (1982): "NASA Airborne Doppler Lidar Program: Data Characteristics of 1981 Wind Field Measurements," Technical Report #1, Prepared for NASA/MSFC under Contract NAS8-34768 by Lassen Research, Manton, Calif. 96059.

ORIGINAL PAGE IS
OF POOR QUALITY

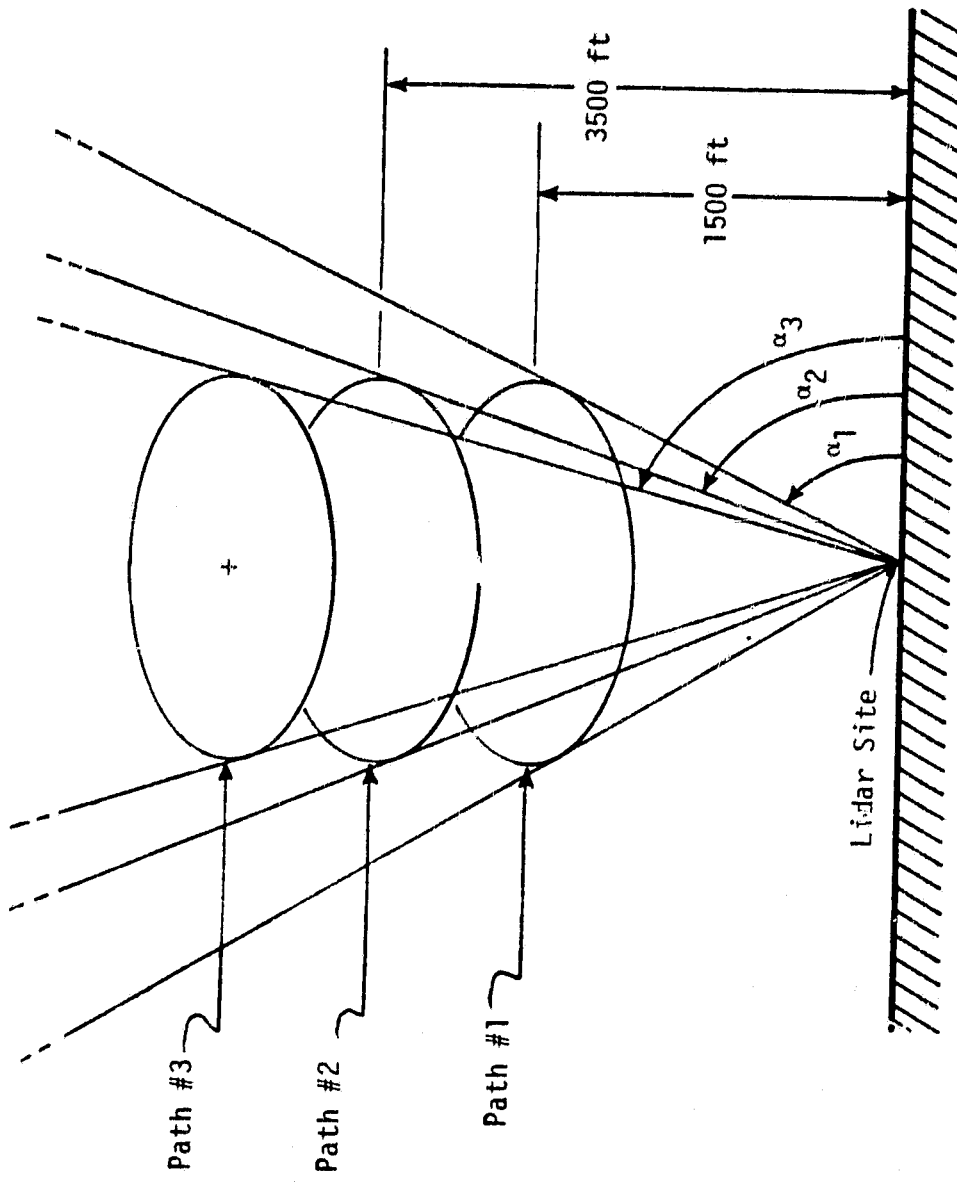


Figure 1 May 10, 1983: RB-57 flight path (aircraft data not currently available for specific details).

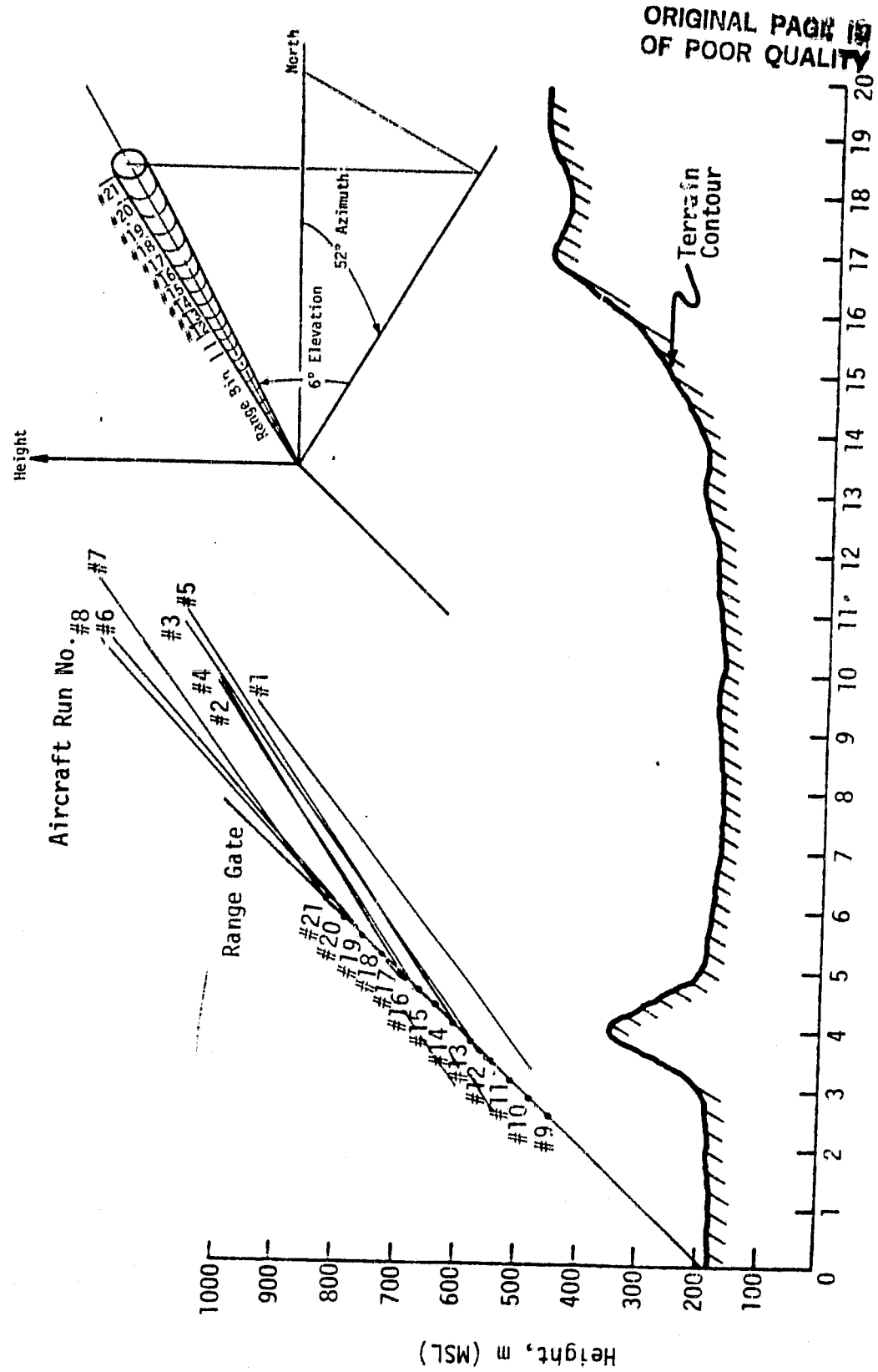


Figure 2 Lidar beam range bins at 6° vertical and 52° azimuth and relative positions of aircraft flight paths.

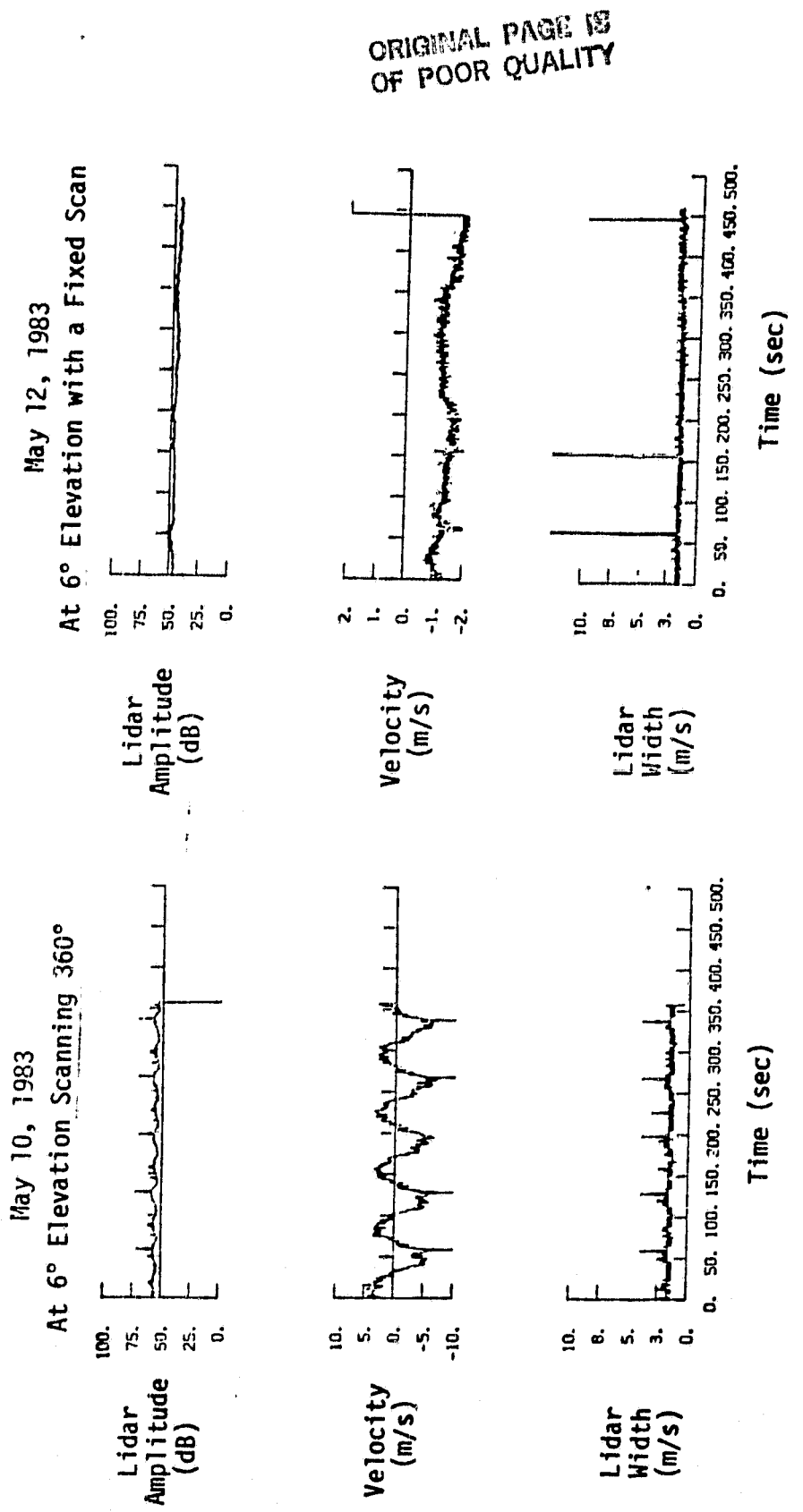


Figure 3 Typical time series of lidar amplitude, velocity, and spectrum width for Range Bin 9.

ORIGINAL PAGE IS
OF POOR QUALITY

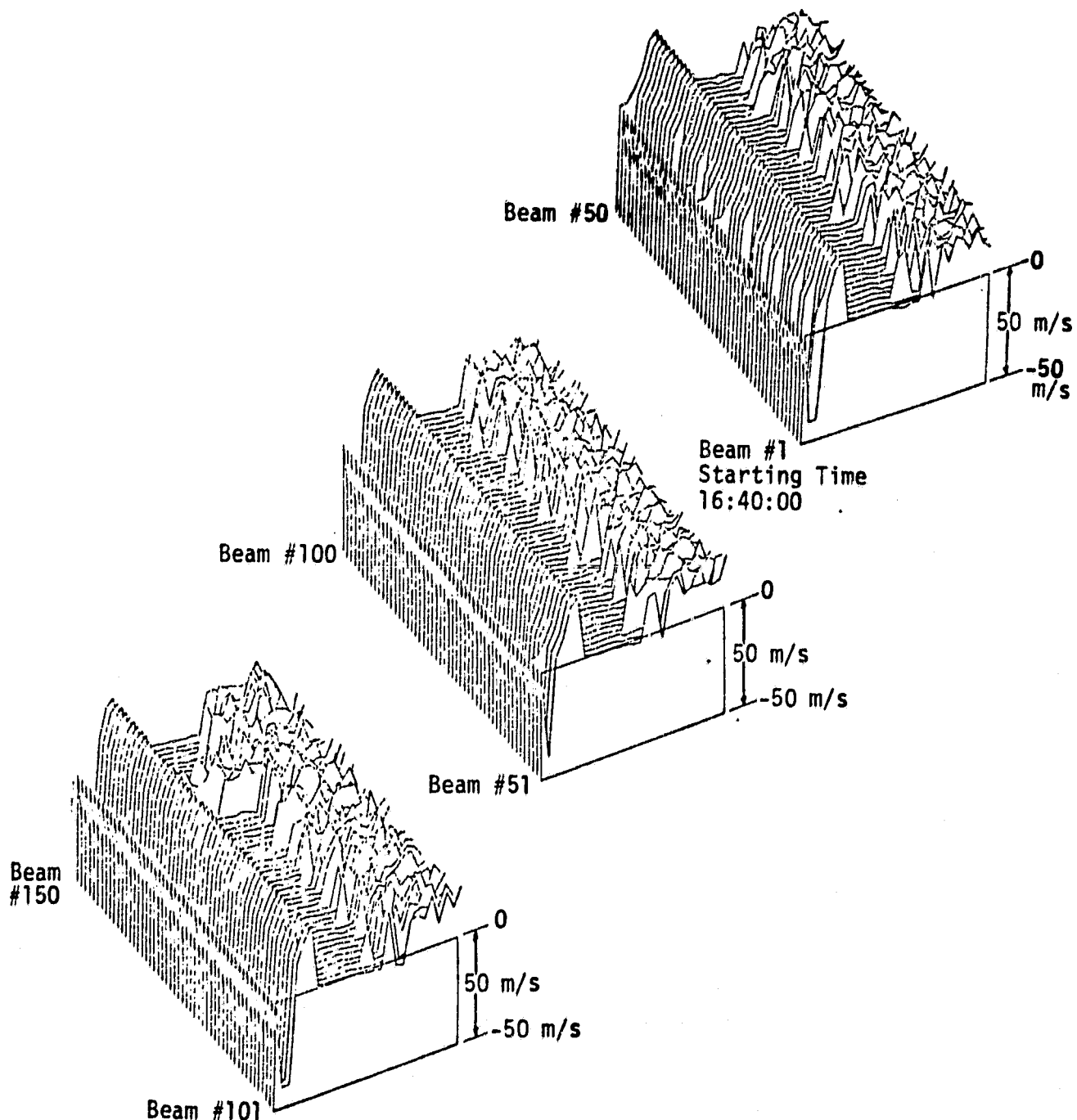
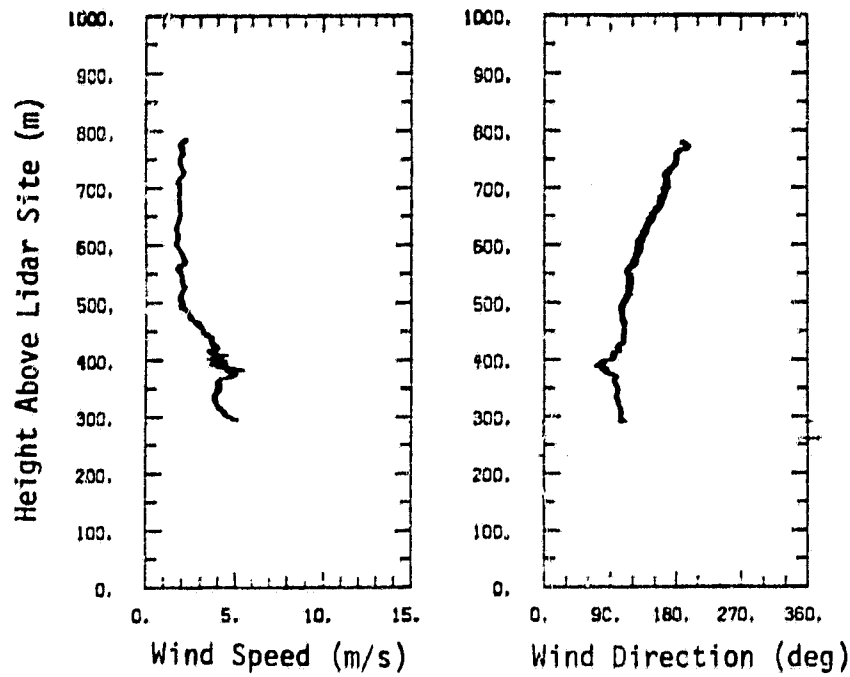
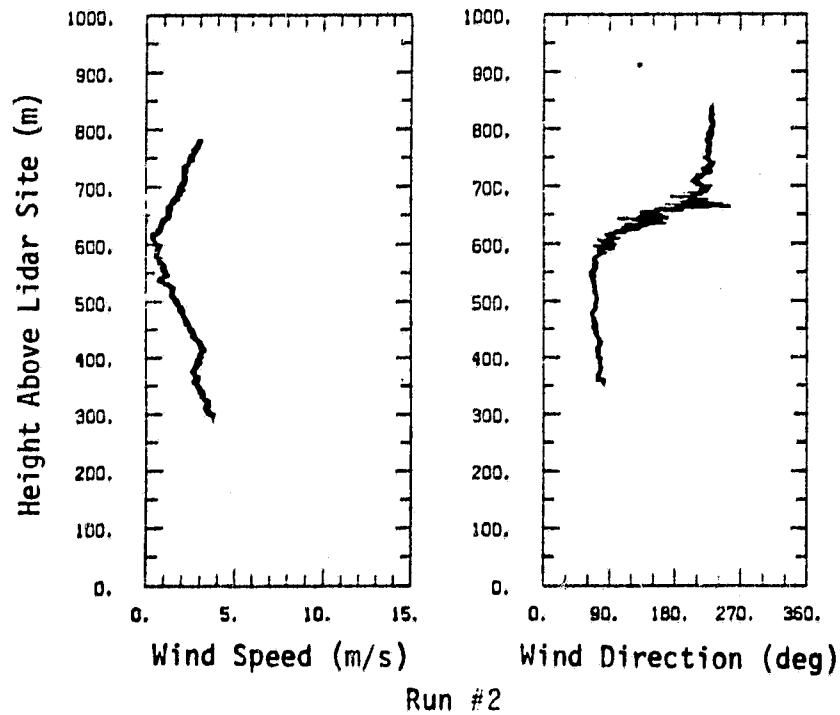


Figure 4 Sample of velocity data along the lidar beam for 150 sequential beams (represents 75 sec of data).

ORIGINAL PAGE IS
OF POOR QUALITY.



Run #1



Run #2

Figure 5 Horizontal wind speed and direction as a function of height (measured from aircraft).

ORIGINAL PAGE IS
OF POOR QUALITY

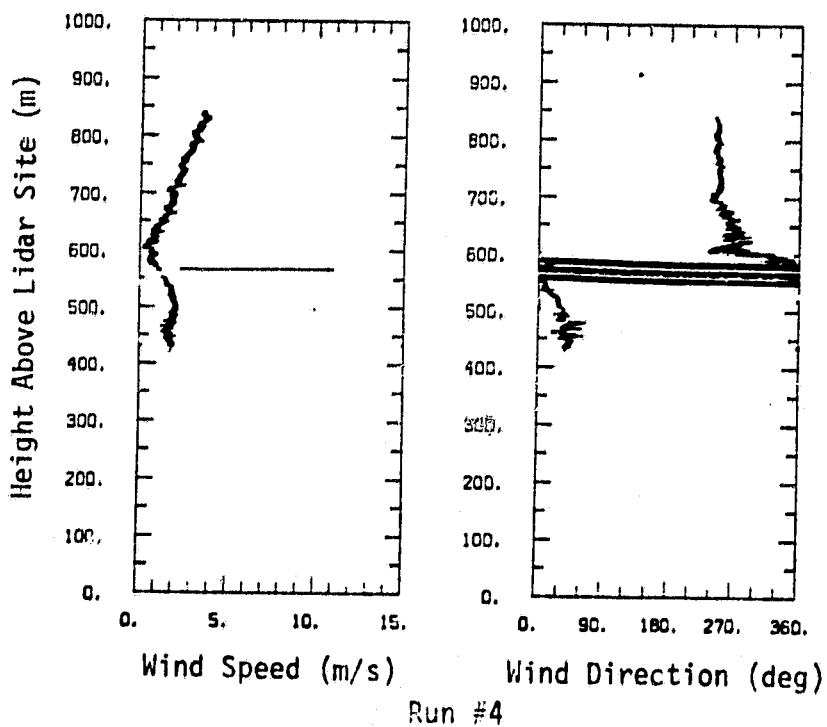
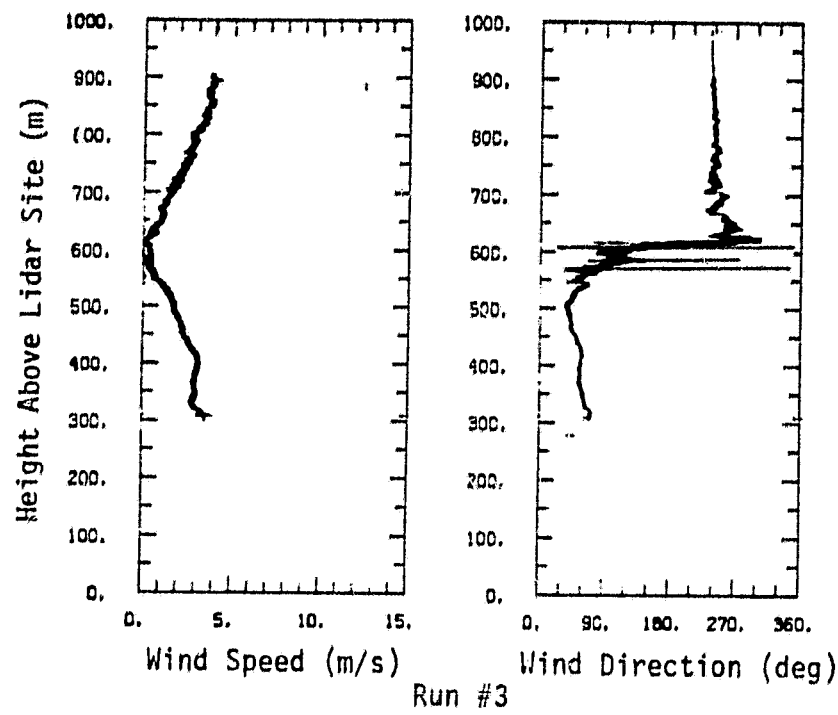


Figure 5 (cont'd).

ORIGINAL PAGE IS
OF POOR QUALITY

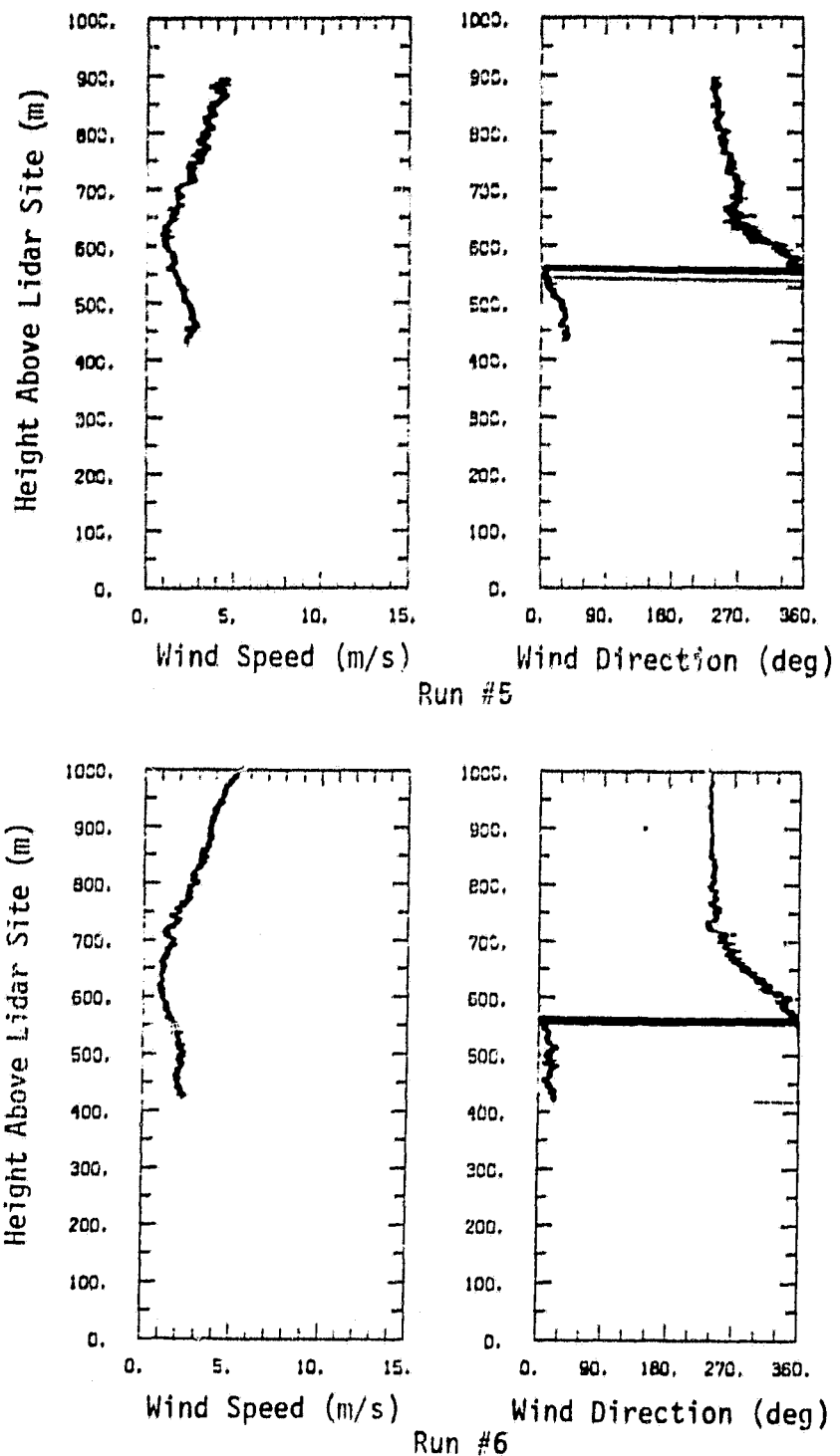


Figure 5 (cont'd.).

ORIGINAL PAGE IS
OF POOR QUALITY

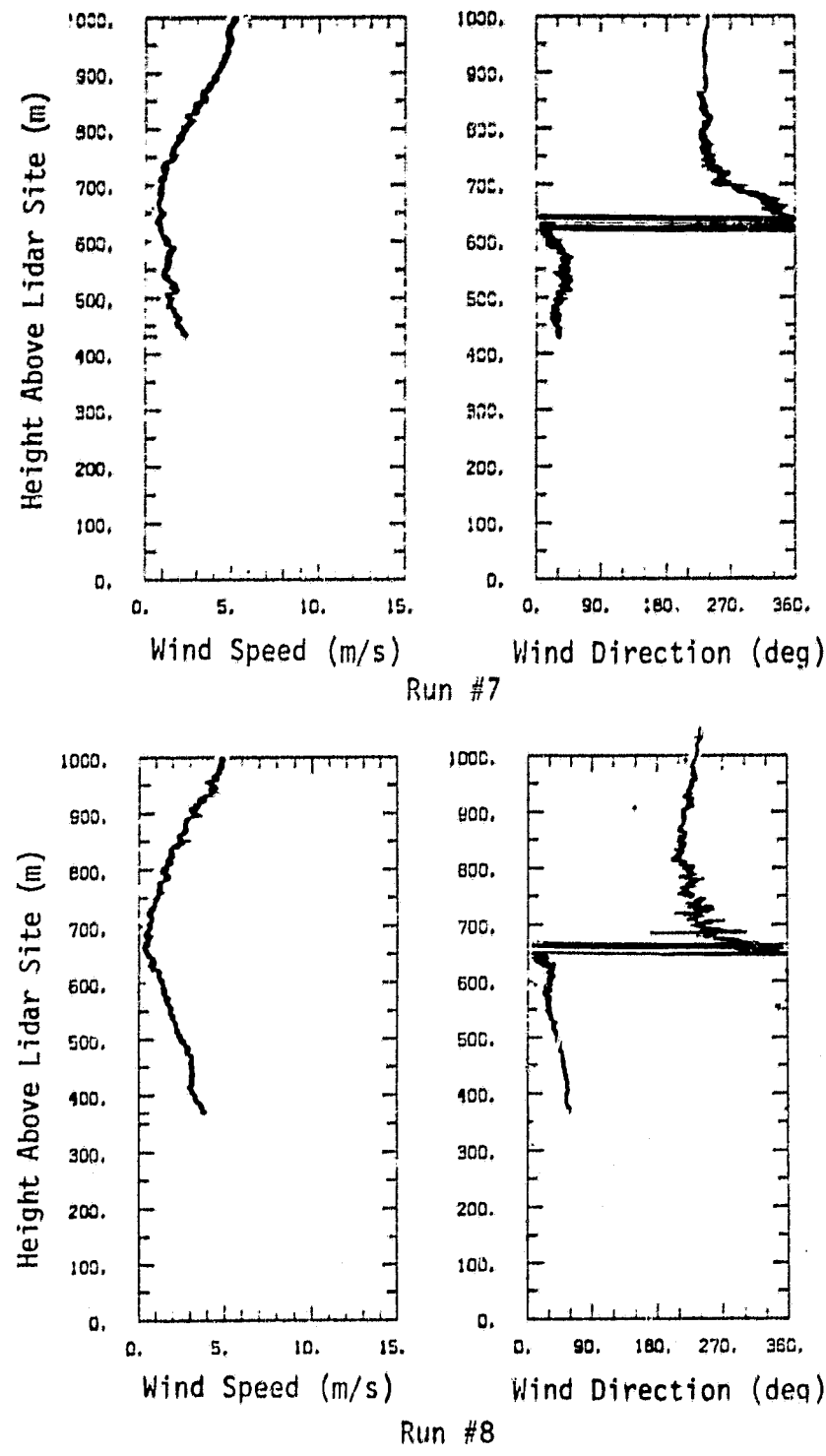


Figure 5 (cont'd).

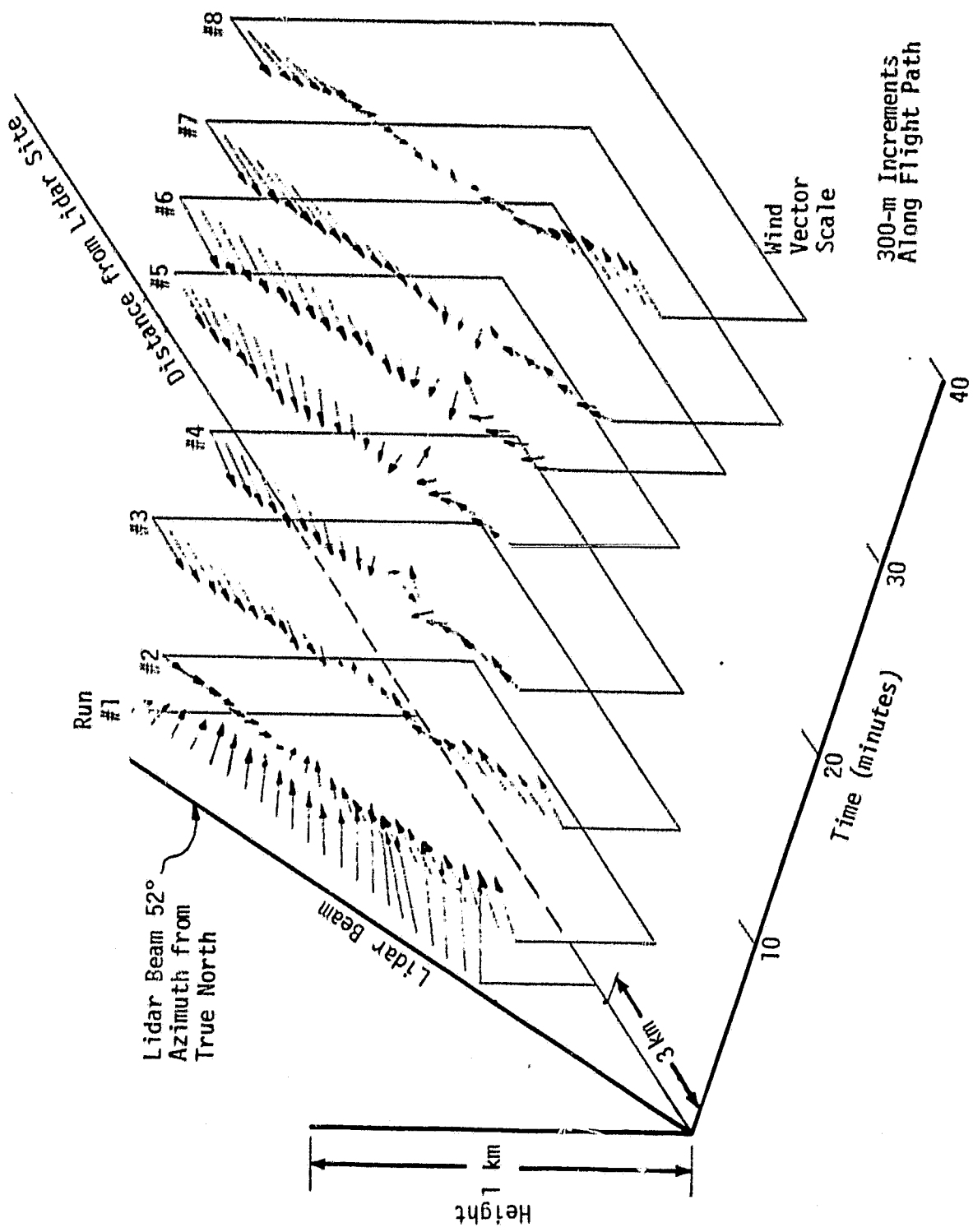


Figure 6 Horizontal wind vectors along RB-57 flight path (May 12, 1983).

ORIGINAL PAGE IS
OF POOR QUALITY

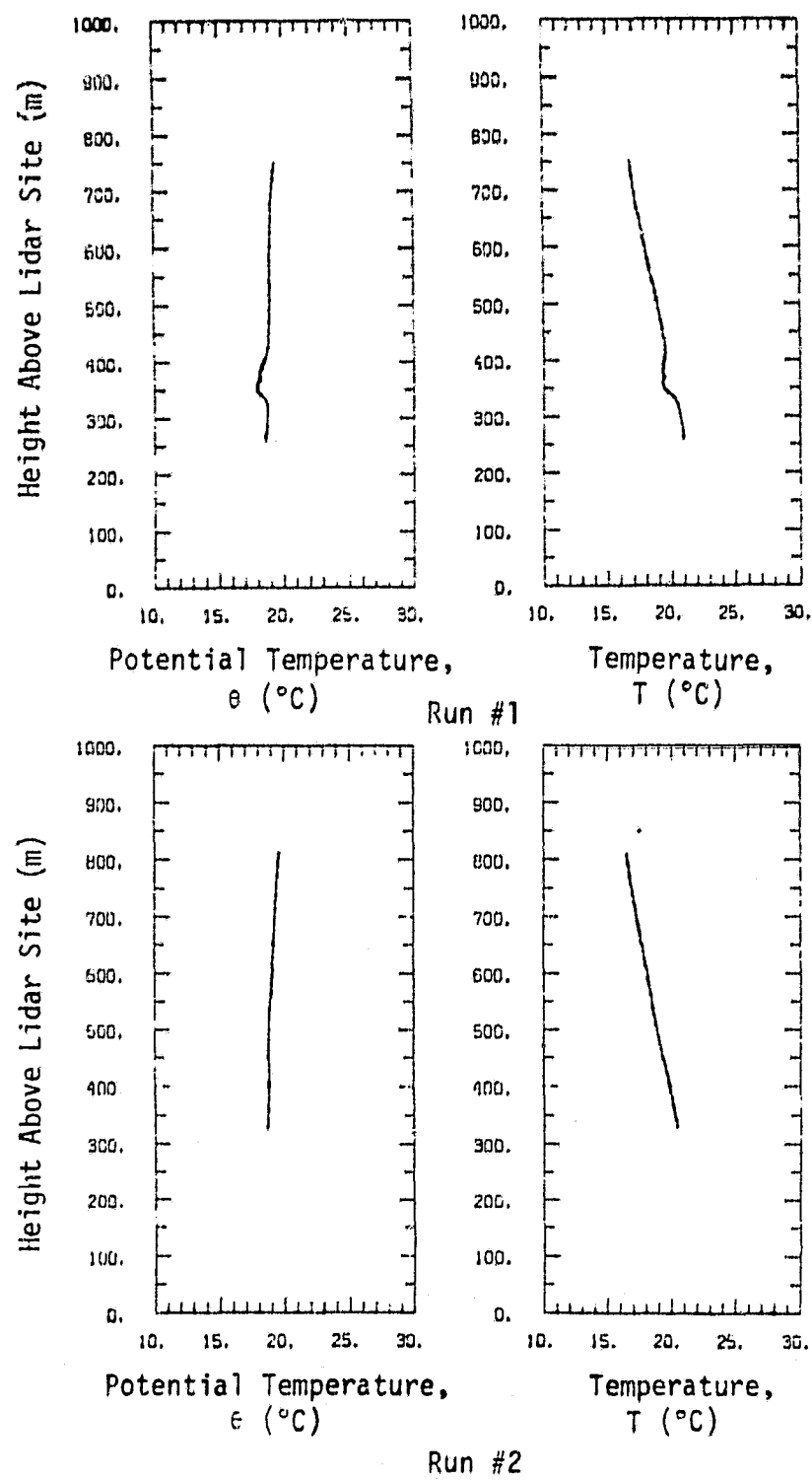


Figure 7 Temperature variations with height.

ORIGINAL PAGE IS
OF POOR QUALITY

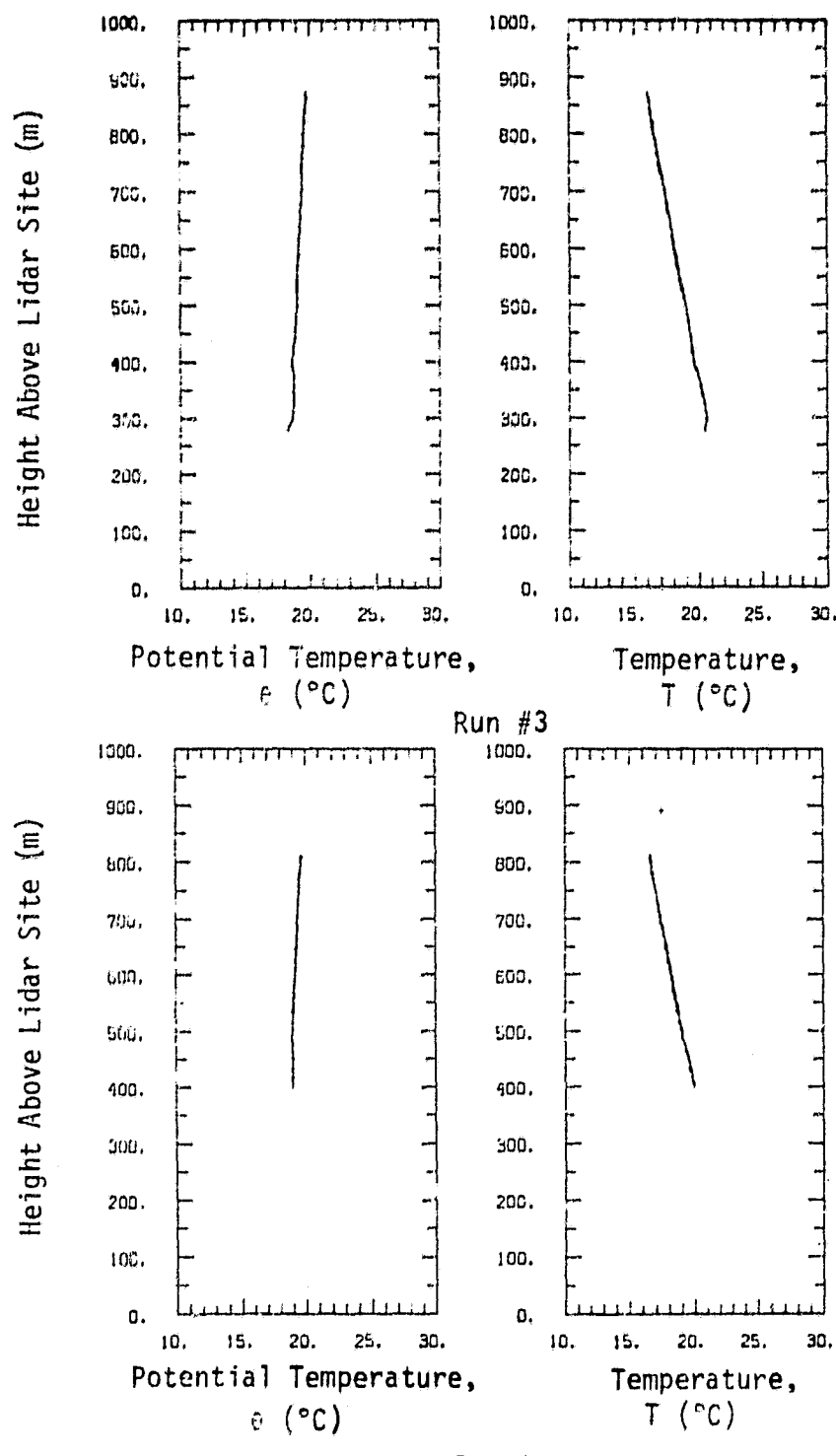


Figure 7 (cont'd.).

ORIGINAL PAGE IS
OF POOR QUALITY

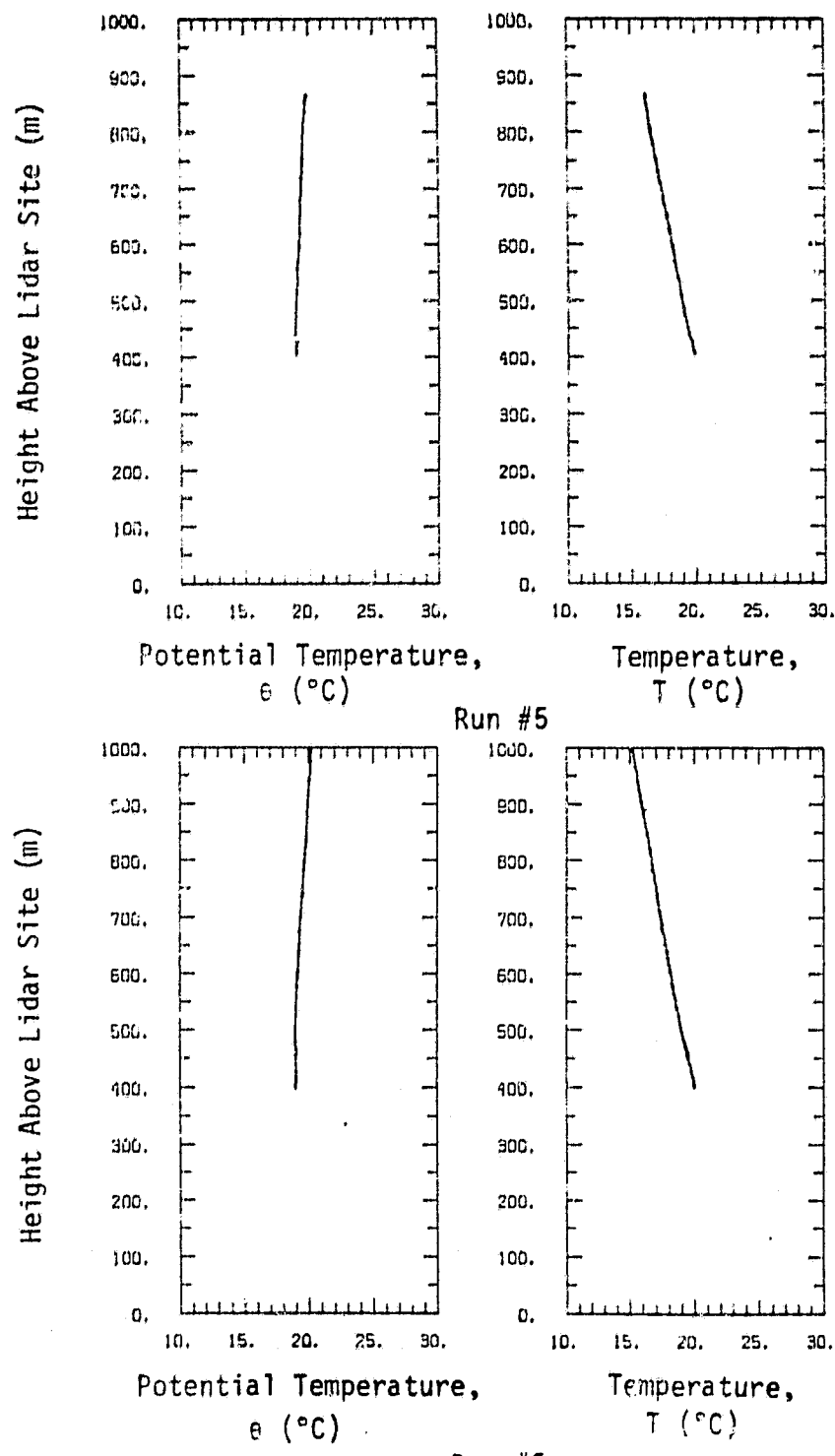


Figure 7 (cont'd.).

ORIGINAL PLATE 16
OF POOR QUALITY

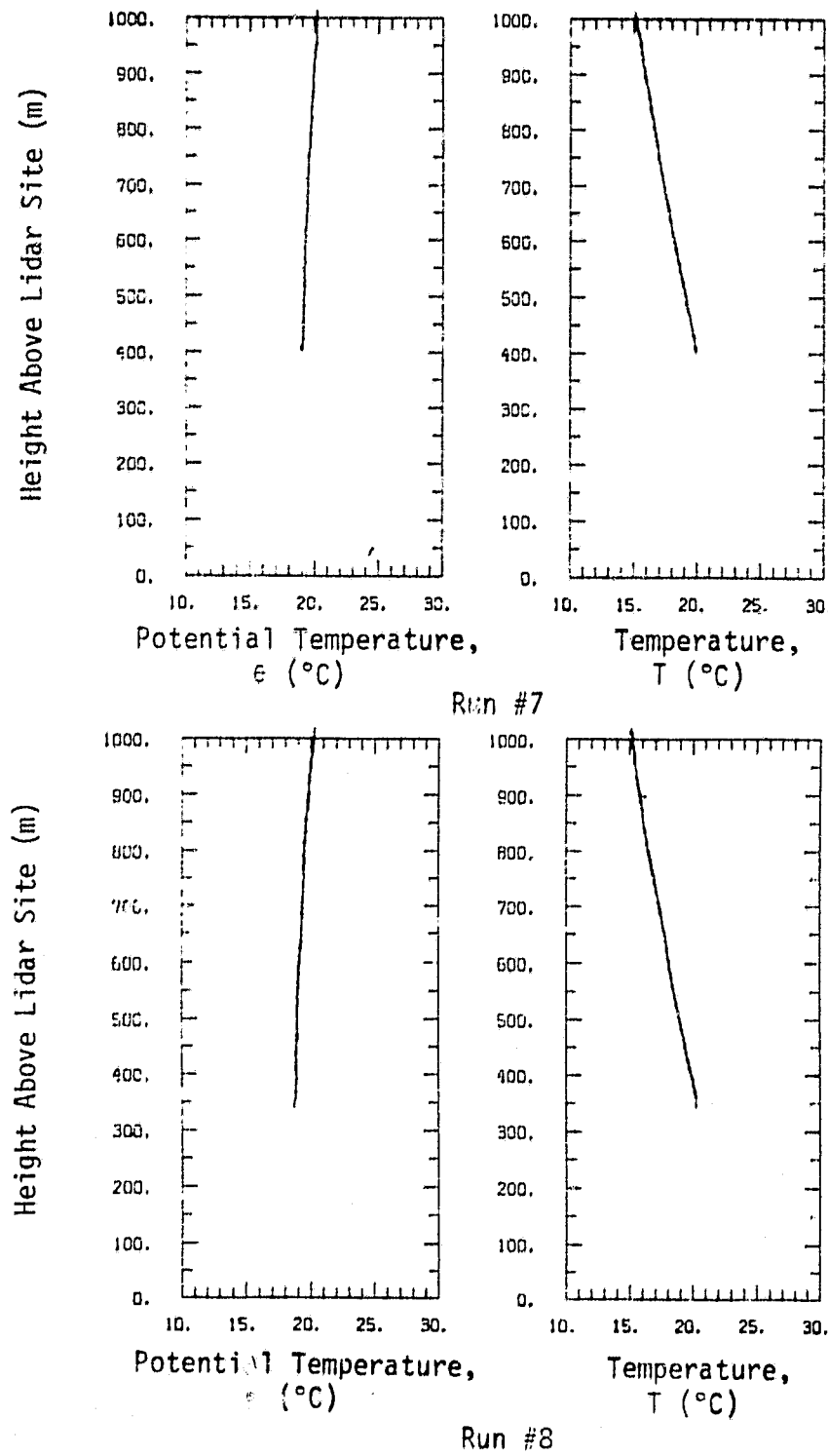


Figure 7 (cont'd).

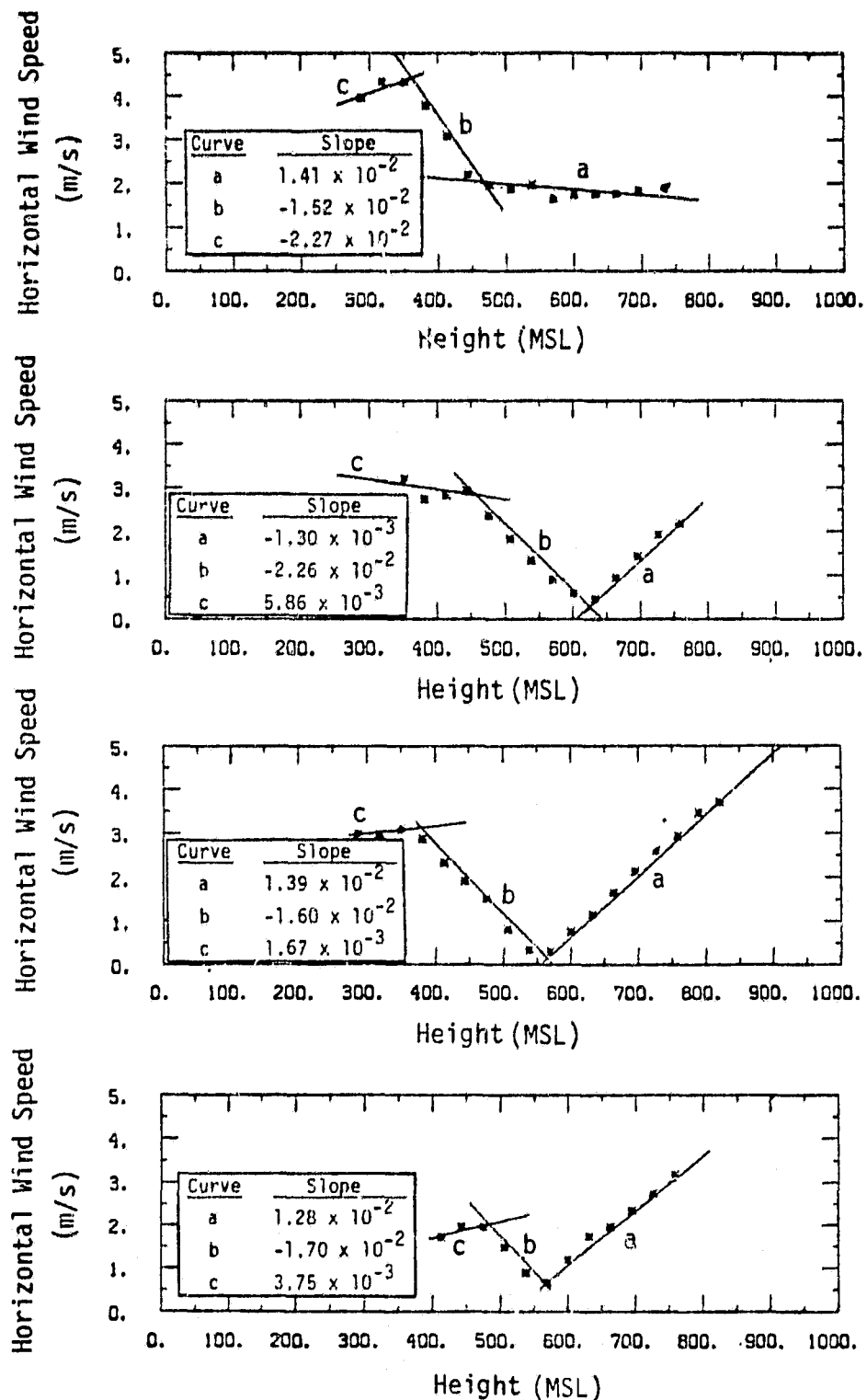


Figure 8 Horizontal wind speed segmented curve fit.

ORIGINAL PAGE IS
OF POOR QUALITY

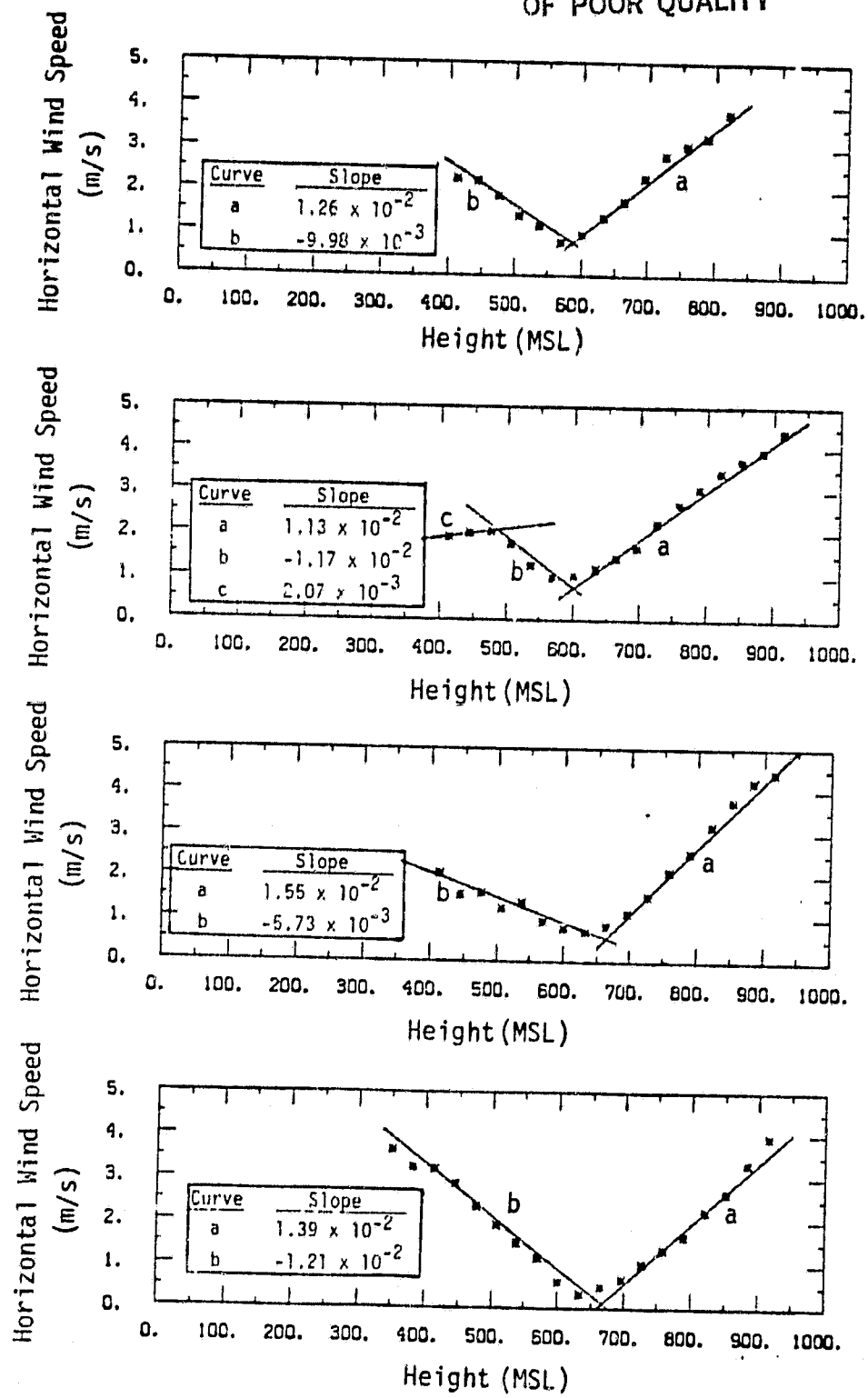


Figure 8 (cont'd.).

ORIGINAL PAGE IS
OF POOR QUALITY

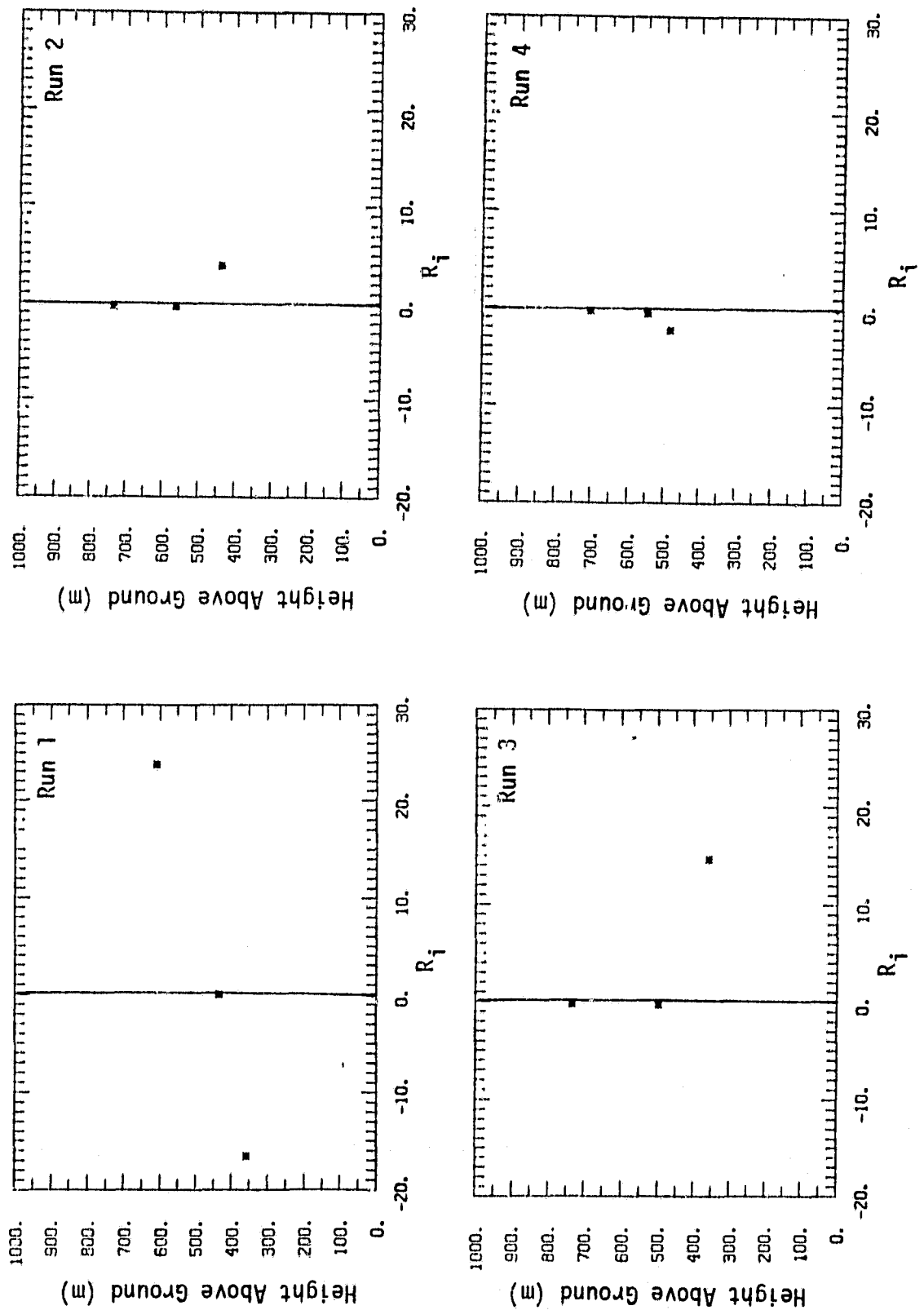


Figure 9 Gradient Richardson number.

CHART 9
OF POOR QUALITY

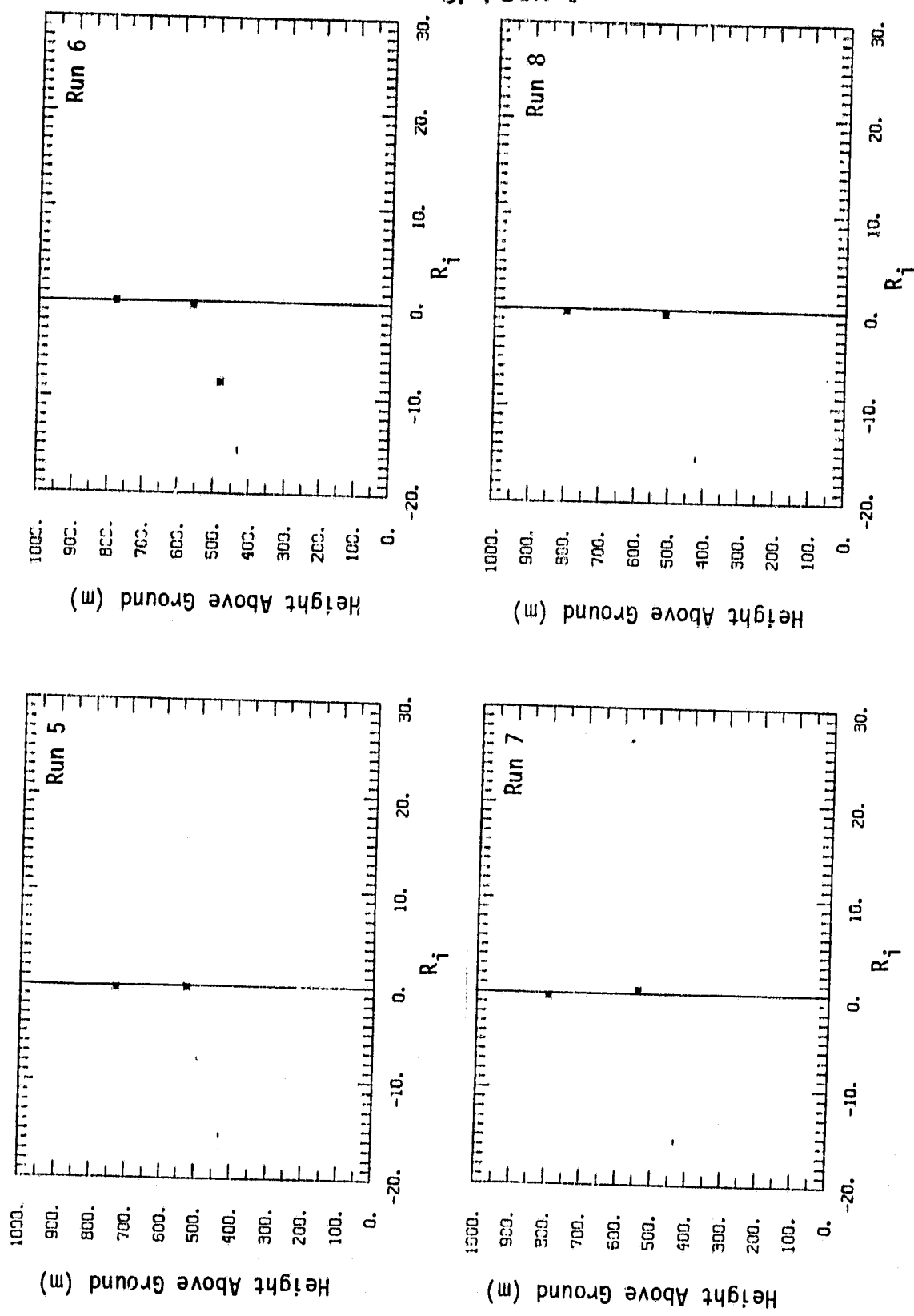


Figure 9 (cont'd.).

ORIGINAL PAGE IS
OF POOR QUALITY

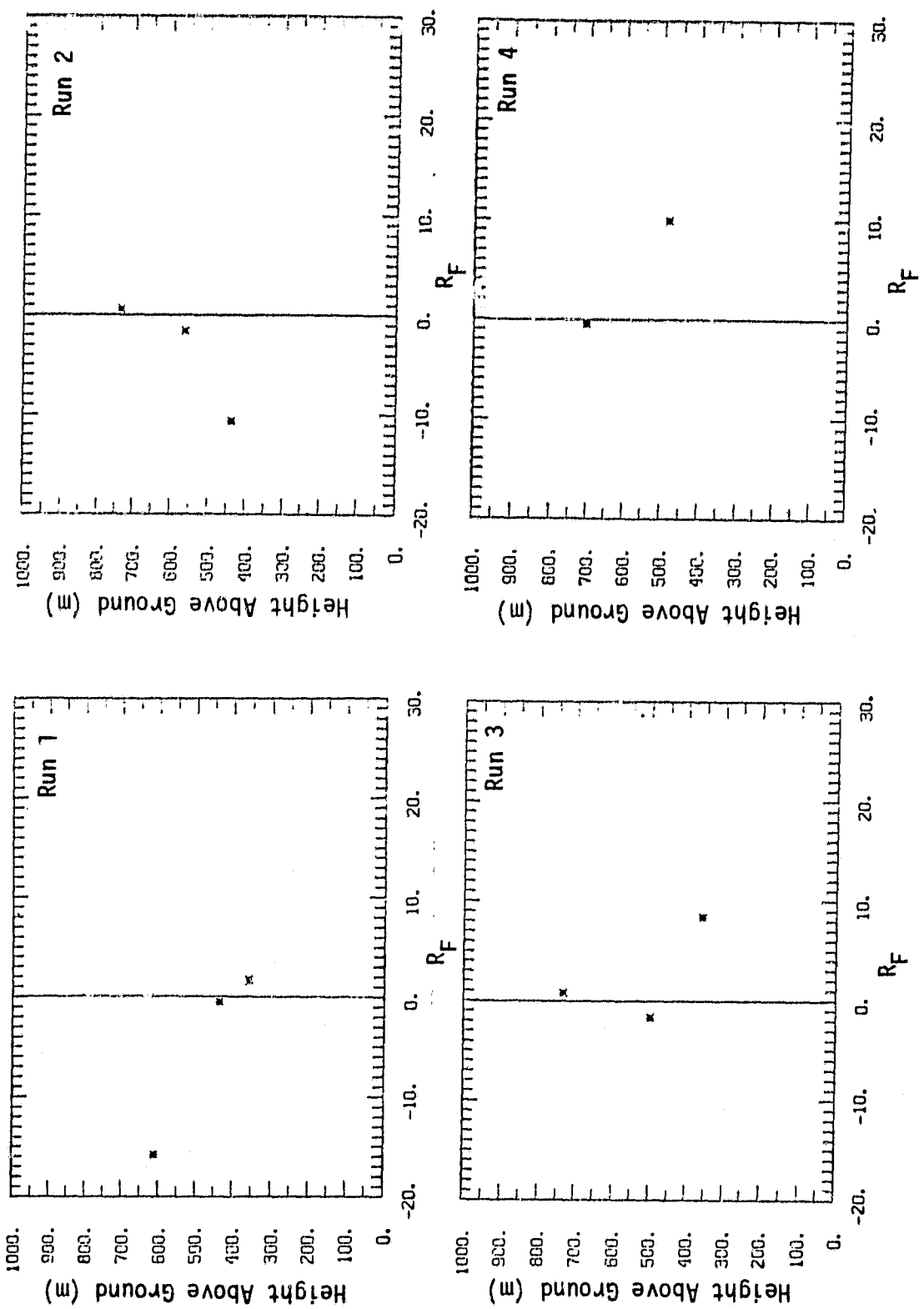


Figure 10 Flux Richardson number.

ORIGINAL PAGE IS
OF POOR QUALITY

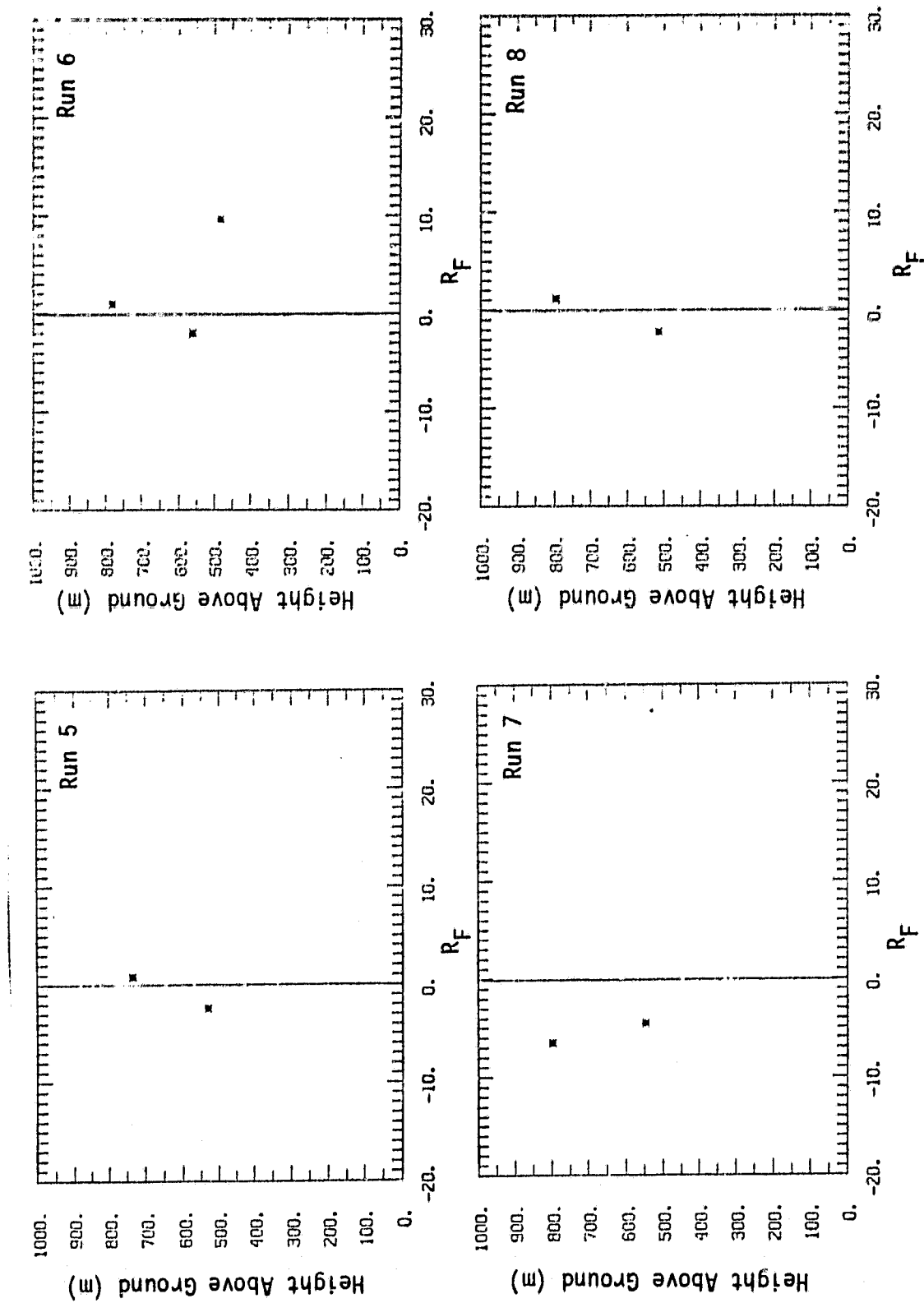
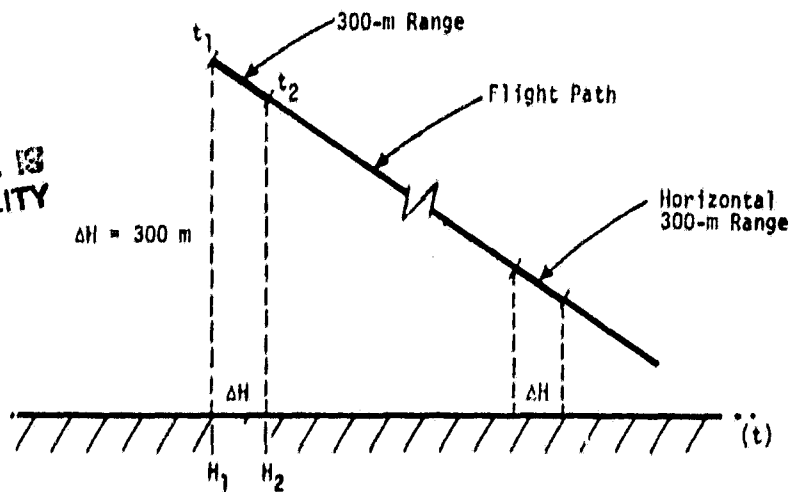


Figure 10 (cont'd.).

ORIGINAL PAGE IS
OF POOR QUALITY



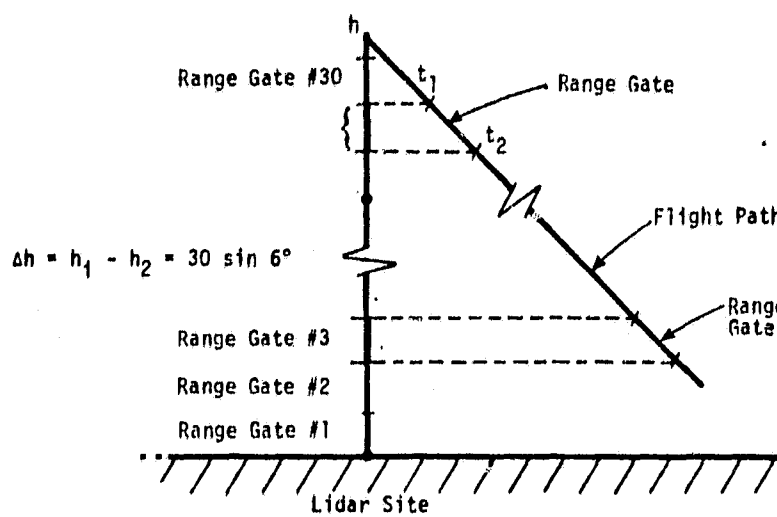
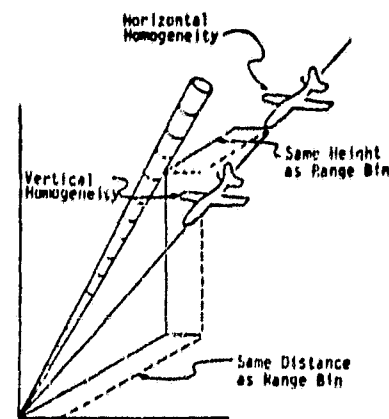
$$\bar{W} = \frac{1}{(N_2 - N_1 + 1)} \sum_{i=N_1}^{N_2} w_i$$

$$N_1 = \frac{t_1 - t_0}{0.025} \quad N_2 = \frac{t_2 - t_0}{0.025}$$

t_0 = beginning of each run

t_1 = time airplane enters each horizontal range at H_1

t_2 = time airplane leaves each horizontal range at H_2



$$\bar{W} = \frac{1}{(N_2 - N_1 + 1)} \sum_{i=N_1}^{N_2} w_i$$

$$N_1 = \frac{t_1 - t_0}{0.025} \quad N_2 = \frac{t_2 - t_0}{0.025}$$

t_0 = beginning of each run

t_1 = time airplane enters each range gate at height h_1

t_2 = time airplane leaves each range gate at height h_2

Figure 11 Evaluation procedure for averaging RB-57 wind for each range bin.

ORIGINAL PAGE IS
OF POOR QUALITY

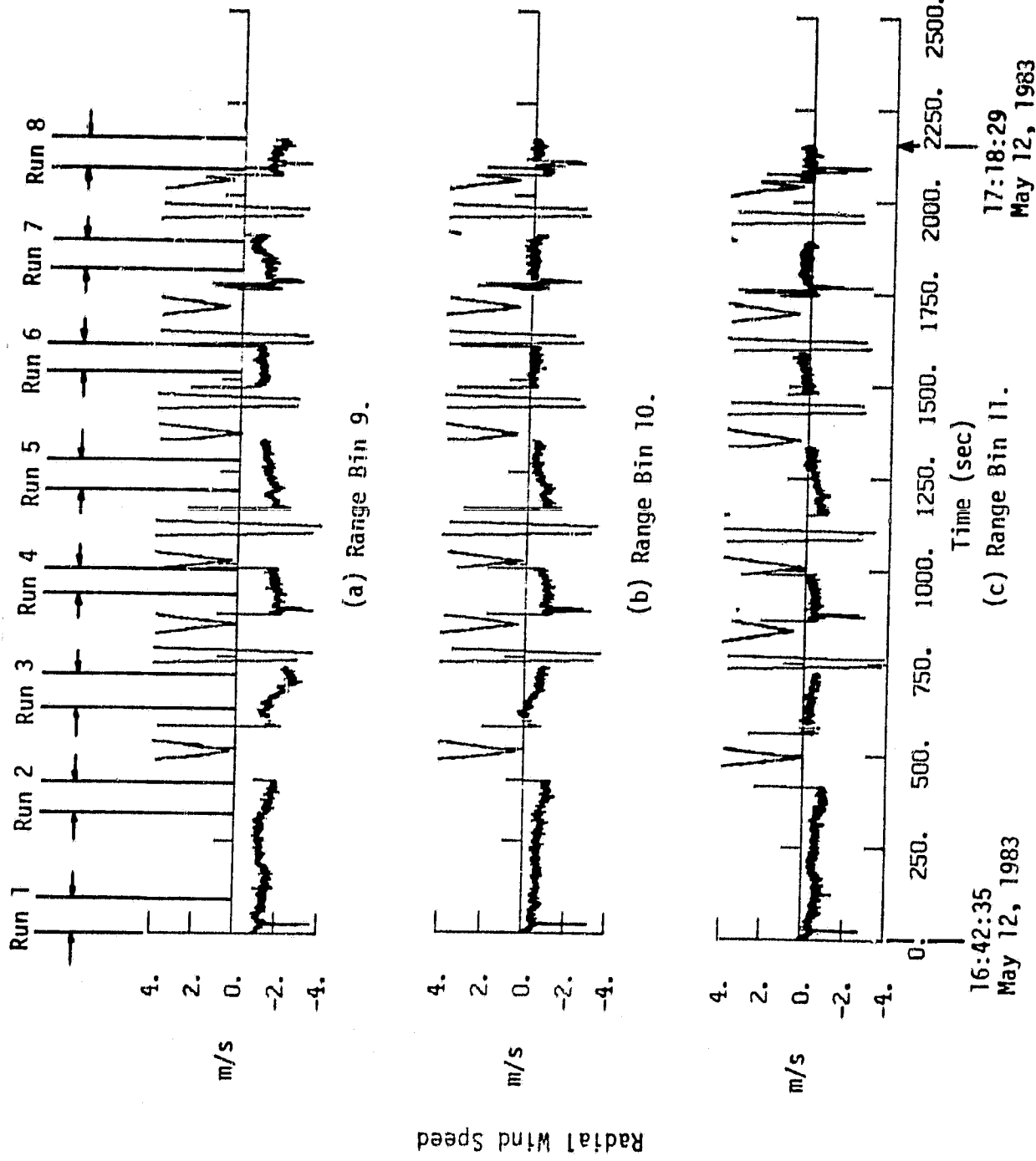
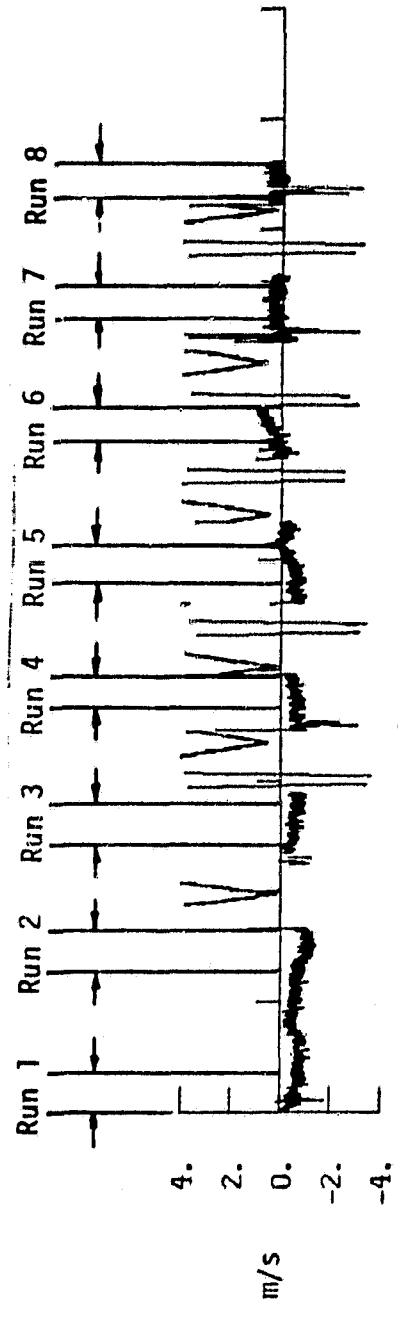
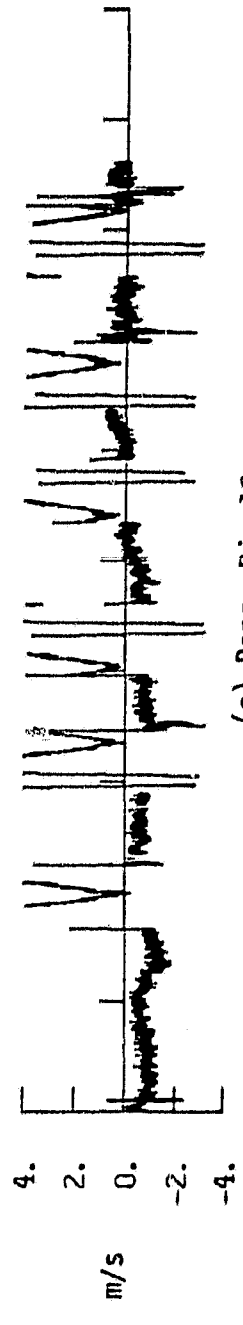


Figure 12 Time histories of radial wind velocity from lidar measurement.

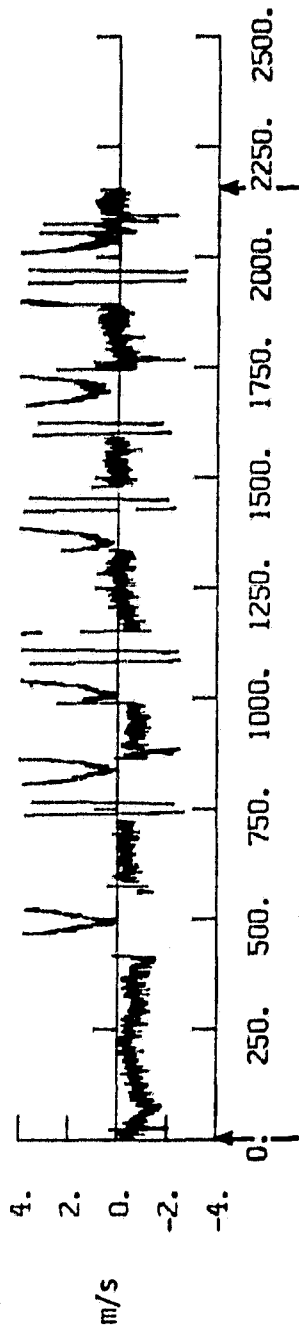
ORIGINAL PAGE IS
OF POOR QUALITY



(d) Range Bin 12.



(e) Range Bin 13.

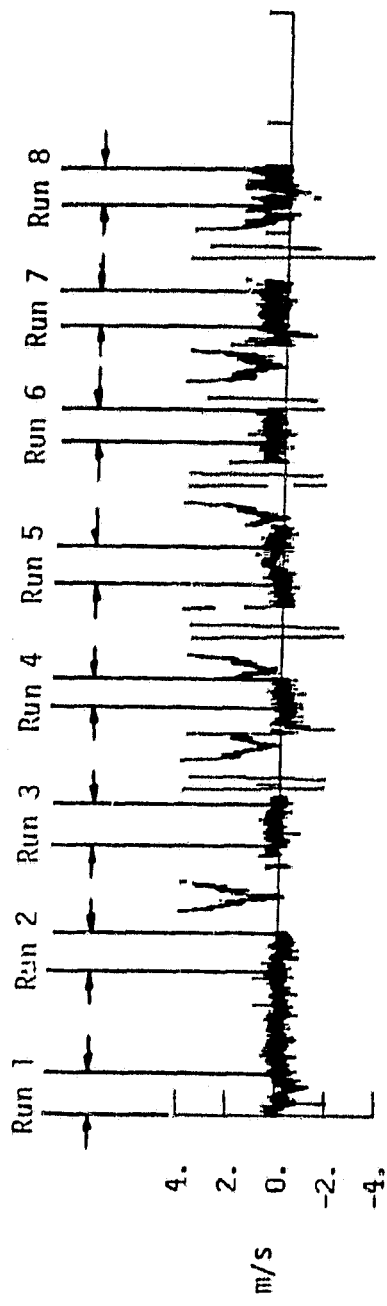


16:42:35
May 12, 1983
17:18:29
May 12, 1983

Figure 12 (cont'd).

Radial Wind Speed

CRISTAL RECORDS
OF POOR QUALITY



(g) Range Bin 15.



(h) Range Bin 16.

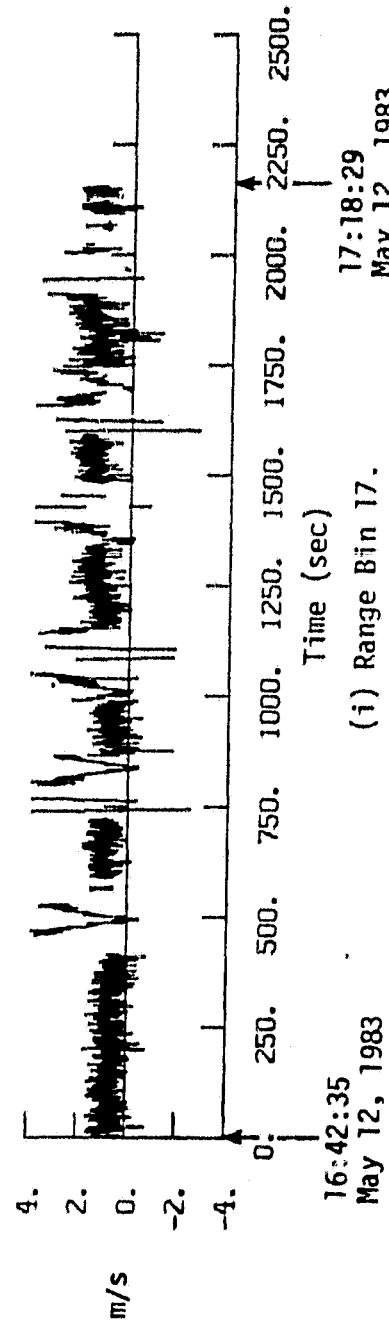
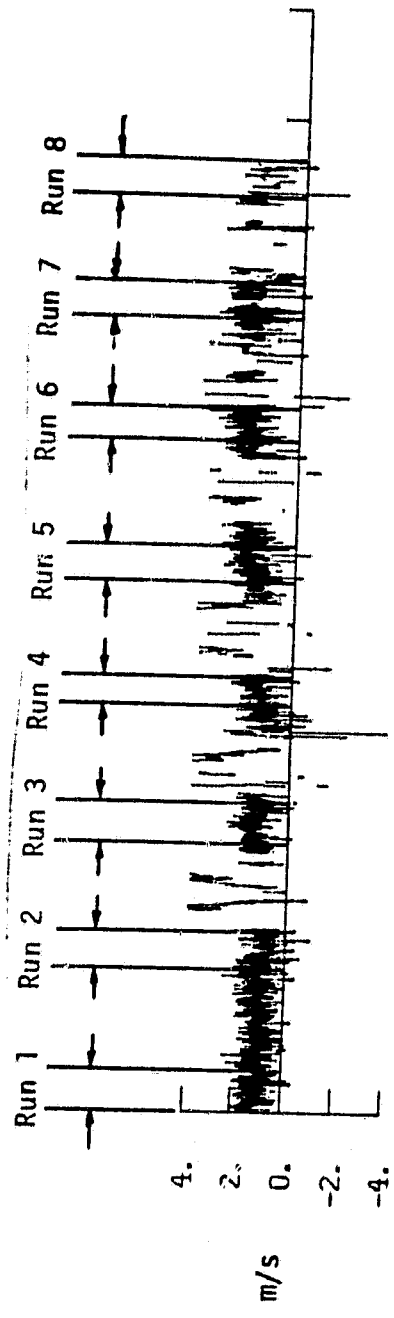
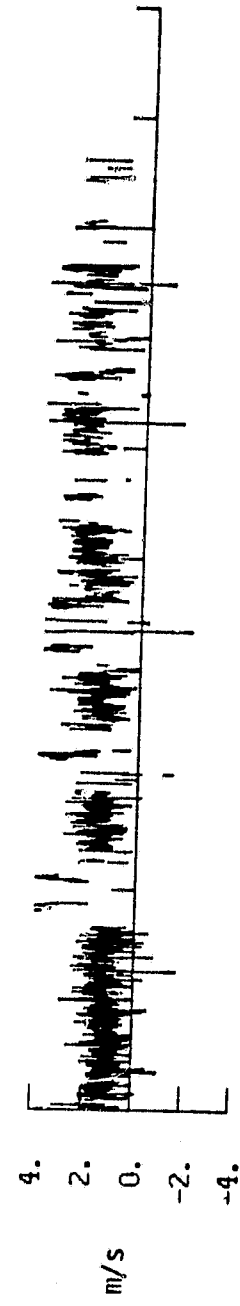


Figure 12 (cont'd).

ORIGINAL PAGE IS
OF POOR QUALITY



(j) Range Bin 18.



(k) Range Bin 19.

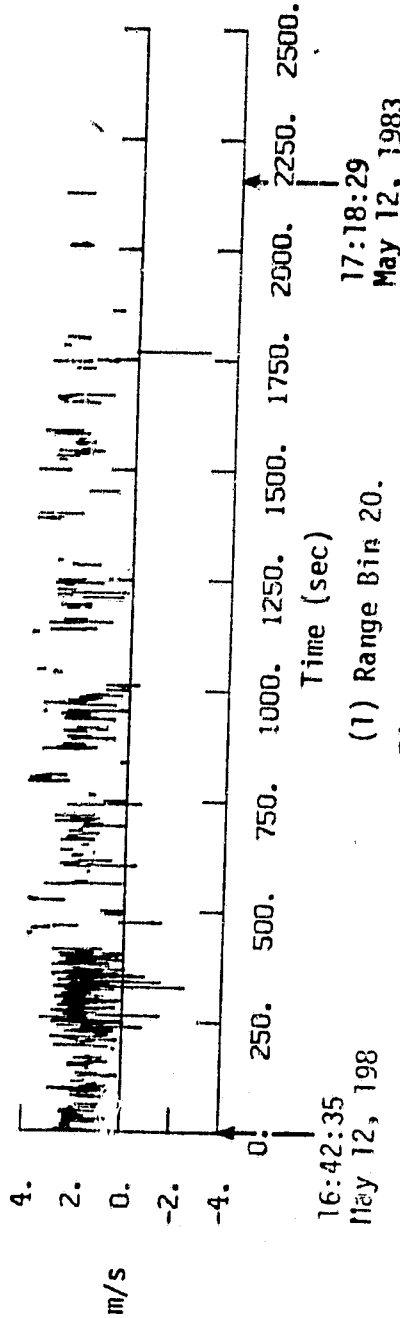


Figure 12 (cont'd).

ORIGINAL PAGE IS
OF POOR QUALITY

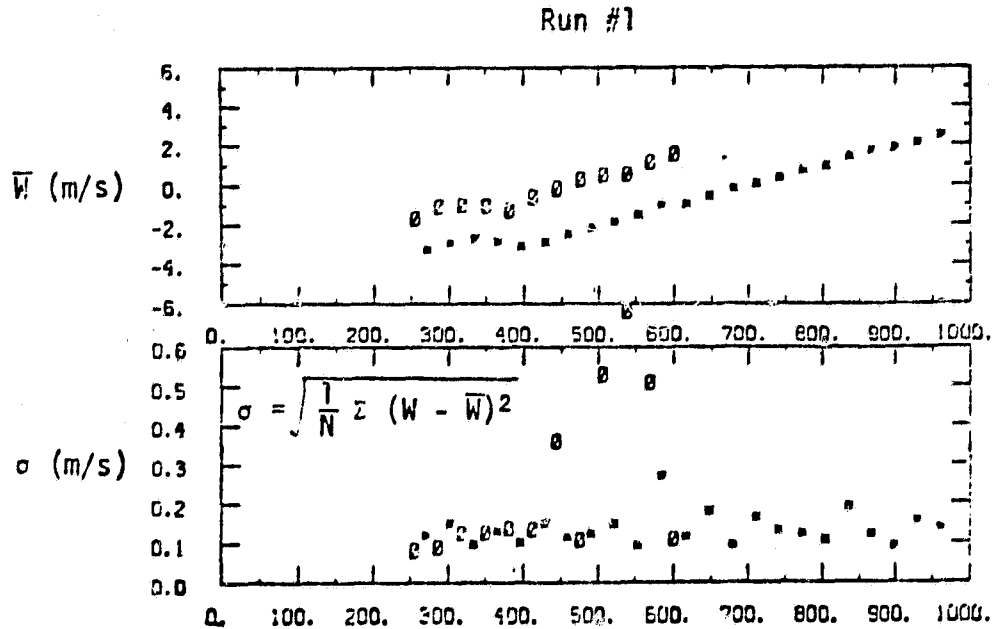
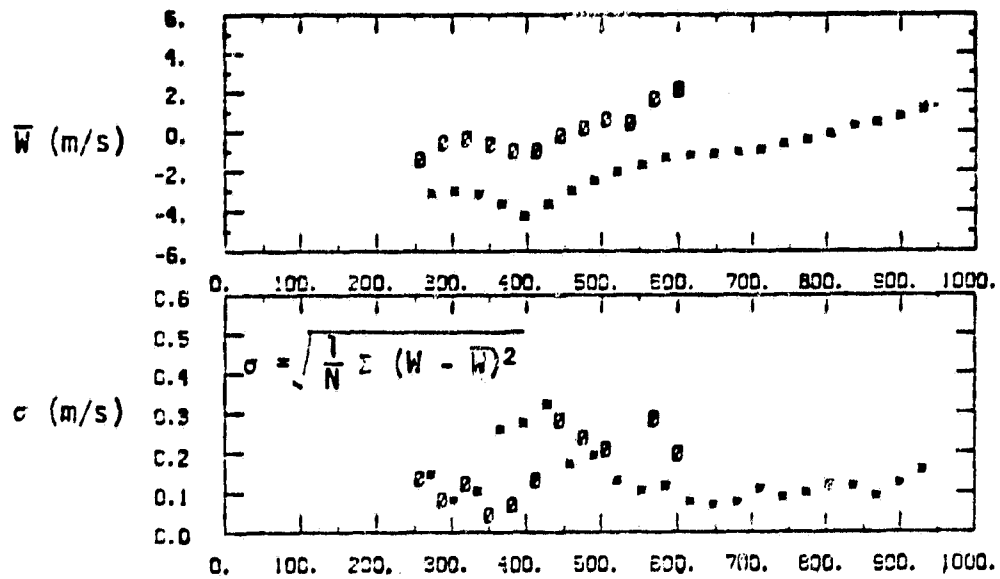
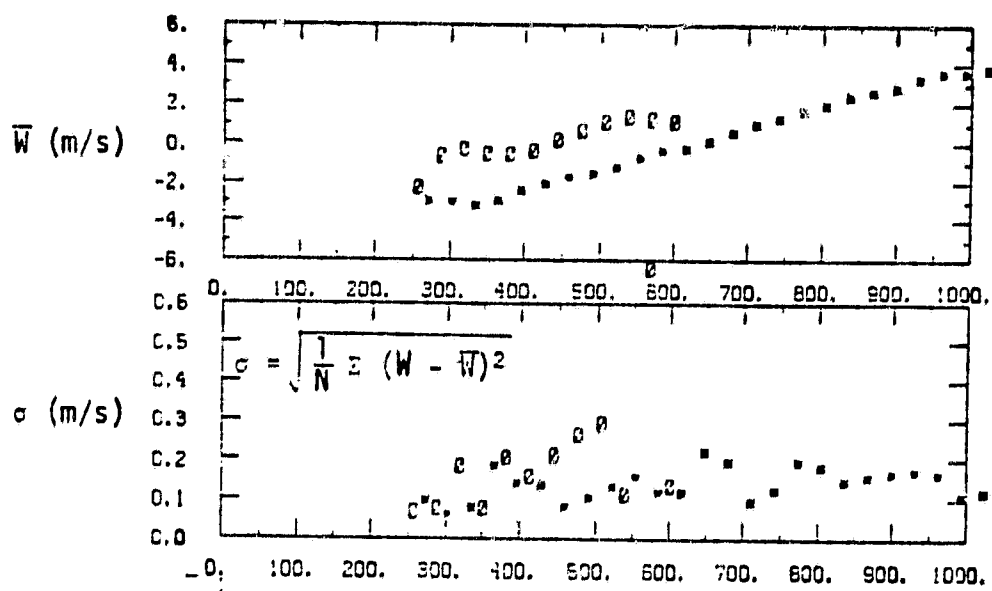
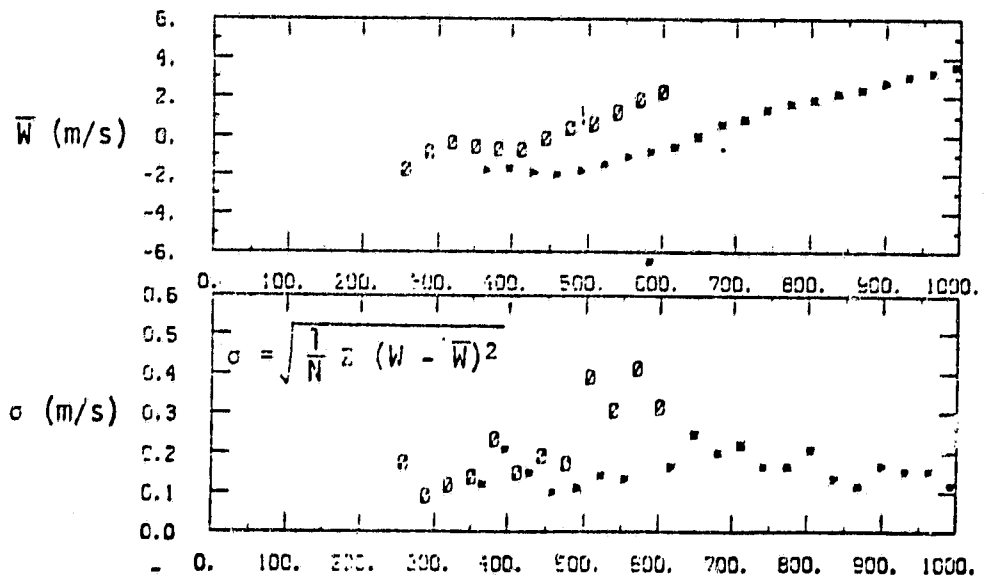


Figure 13 Comparison of lidar-measured winds with aircraft-measured winds and computed turbulence (assumed vertical homogeneity); aircraft = x, Lidar = \emptyset .

ORIGINAL PAGE IS
OF POOR QUALITY



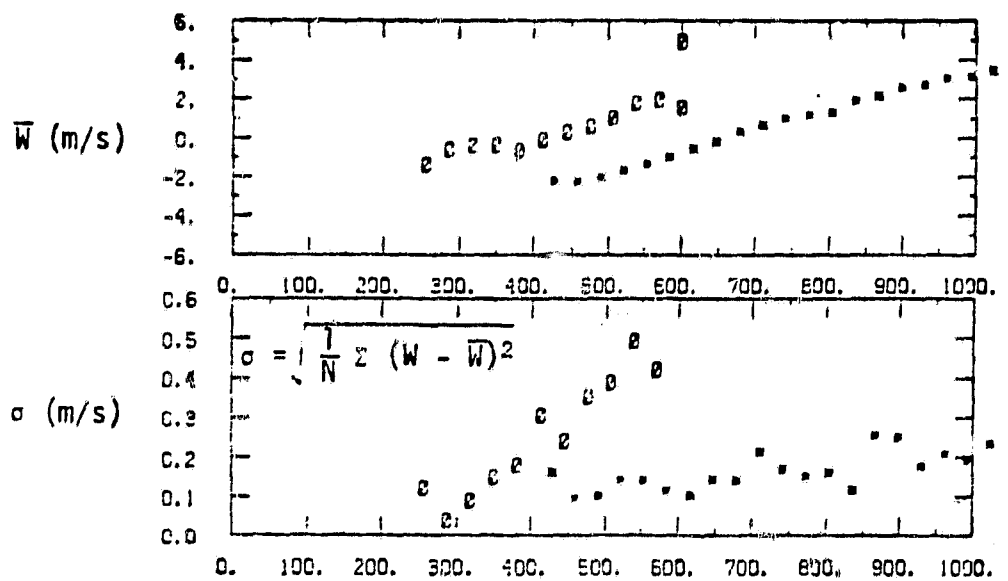
Run #3



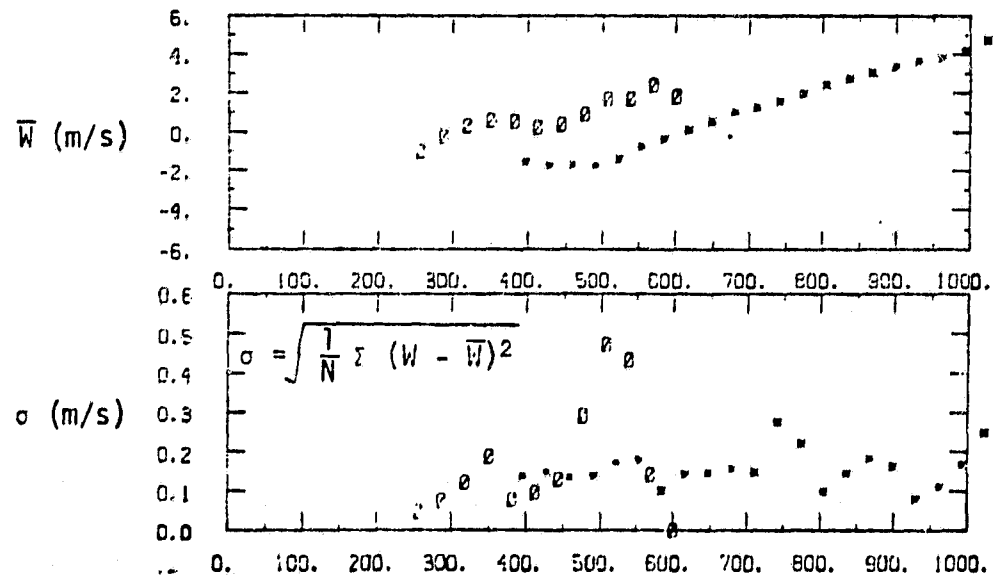
Run #4

Figure 13 (cont'd).

ORIGINAL PAGE IS
OF POOR QUALITY



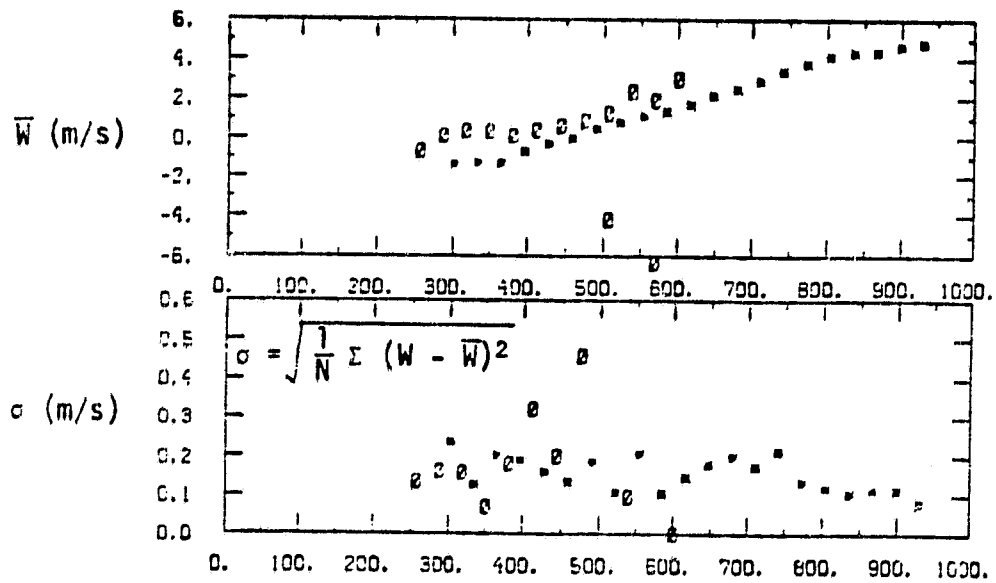
Run #5



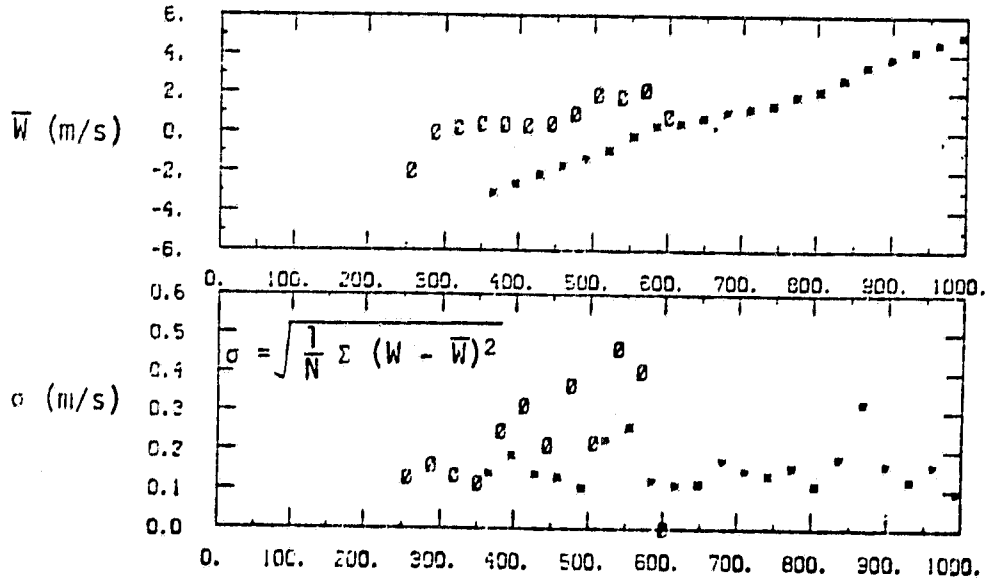
Run #6

Figure 13 (cont'd).

ORIGINAL PAGE IS
OF POOR QUALITY



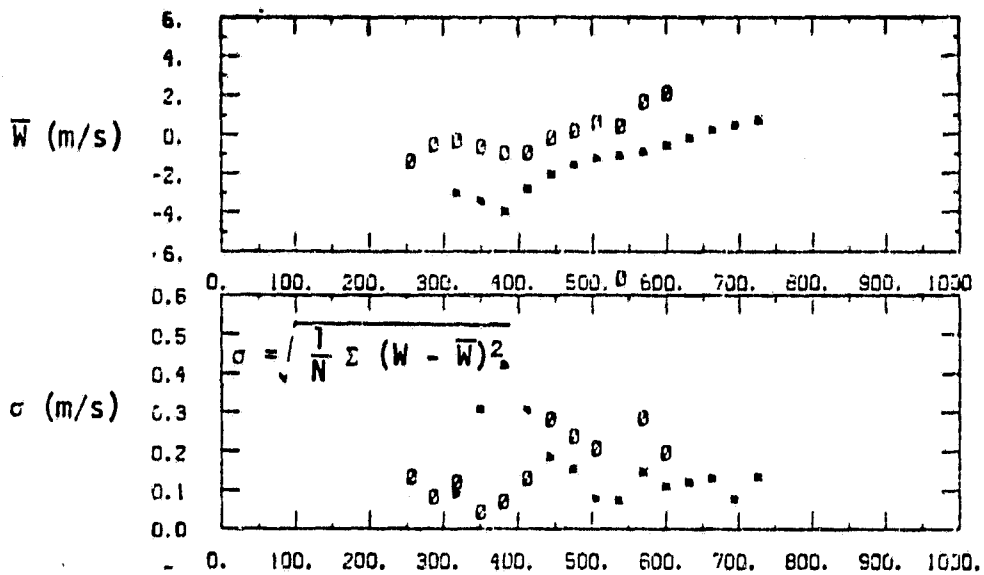
Run #7



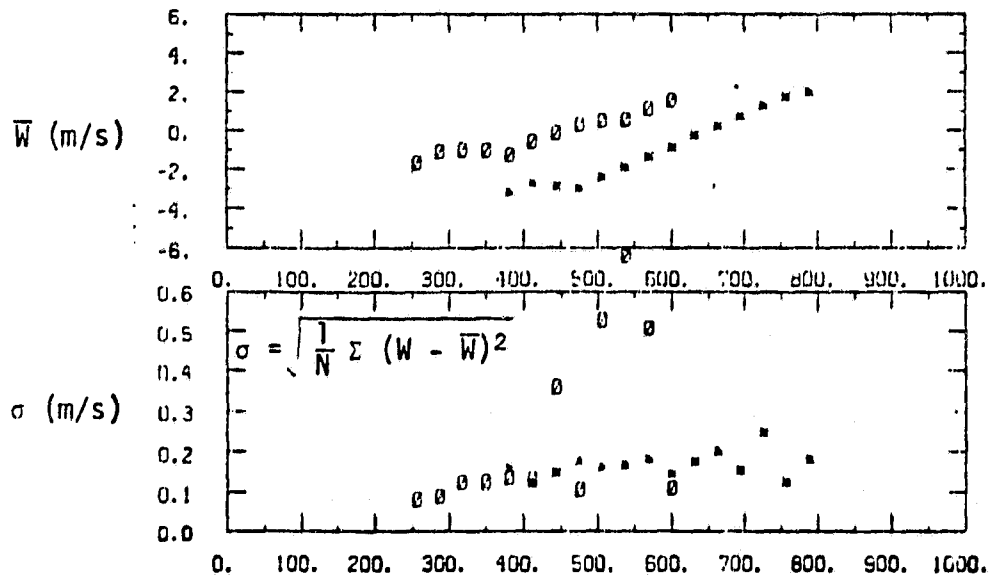
Run #8

Figure 13 (cont'd.).

ORIGINAL PAGE IS
OF POOR QUALITY



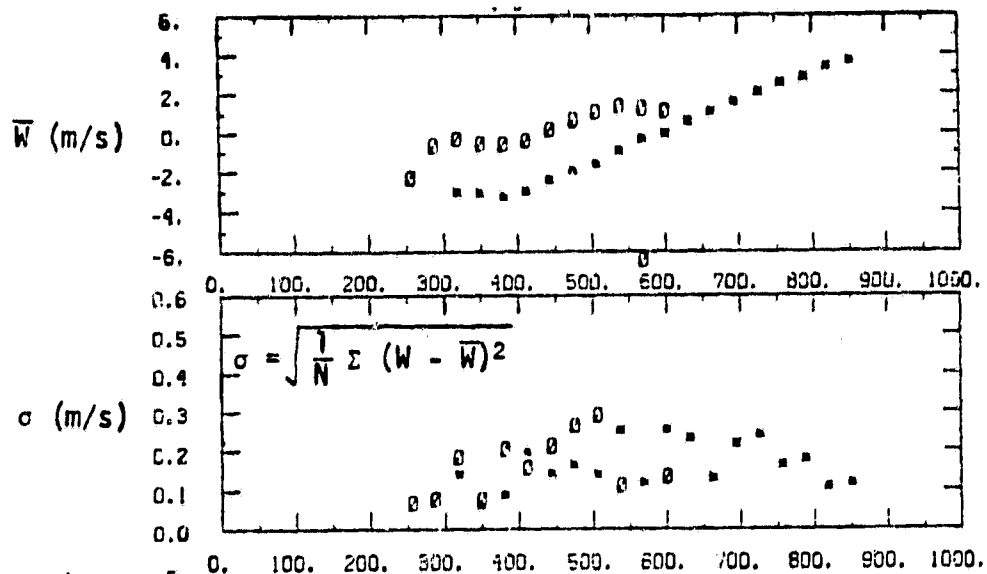
Run #1



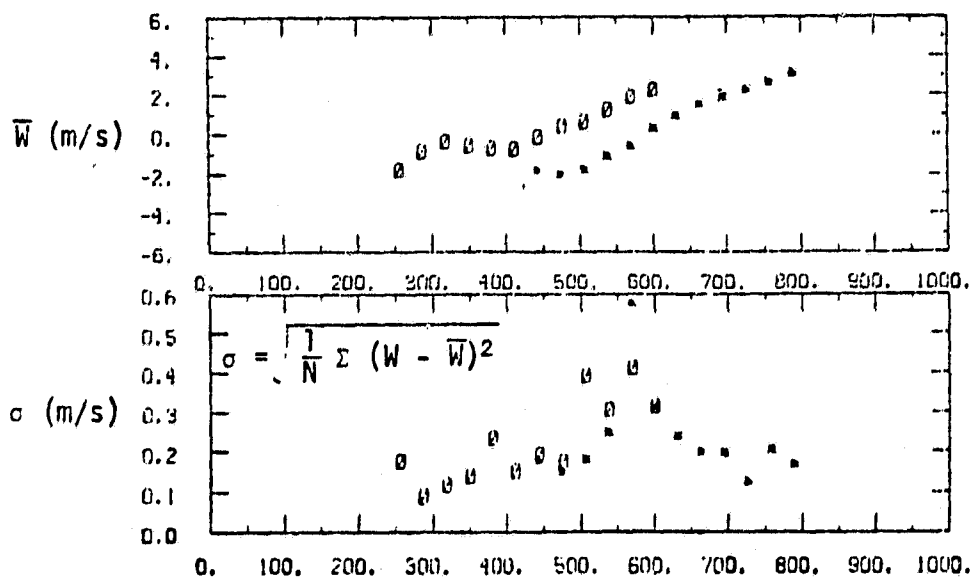
Run #2

Figure 14 Comparison of lidar-measured winds with aircraft-measured winds and computed turbulence (assumed horizontal homogeneity); Aircraft = x, Lidar = θ .

ORIGINAL PAGE IS
OF POOR QUALITY



Run #3



Run #4

Figure 14 (cont'd).

ORIGINAL PAGE IS
OF POOR QUALITY

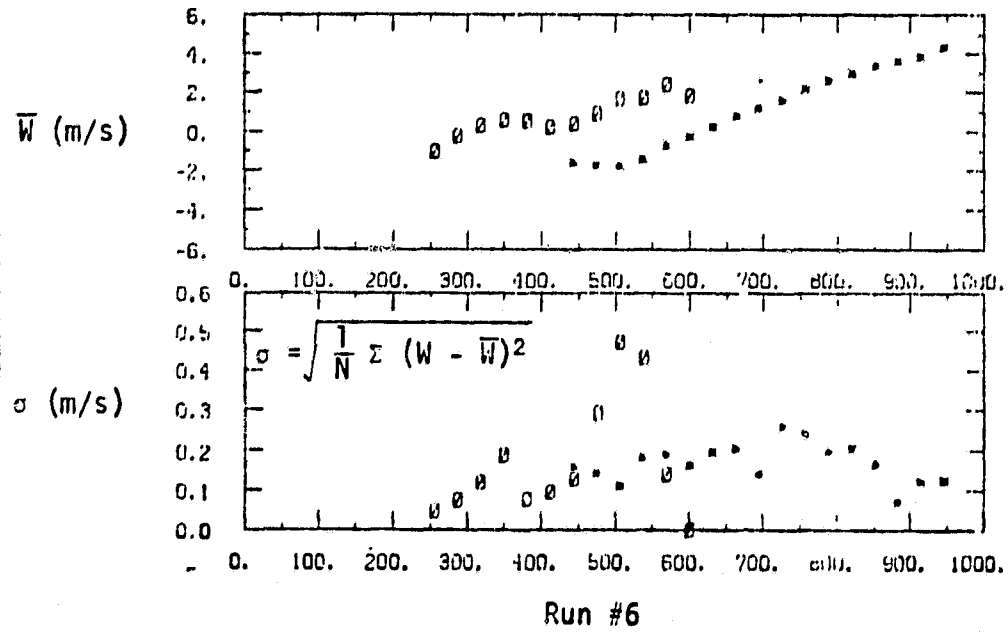
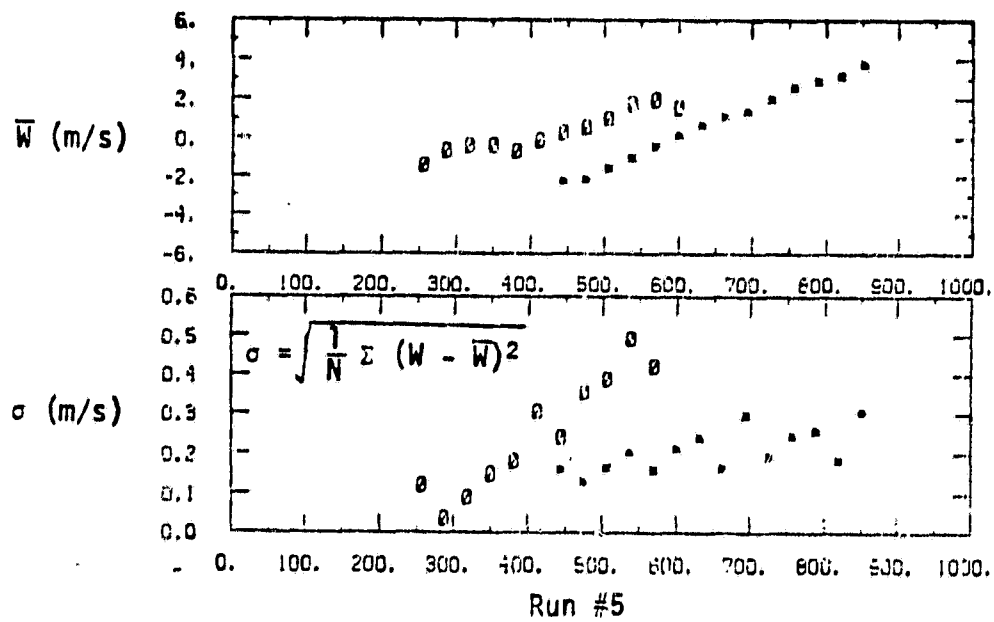
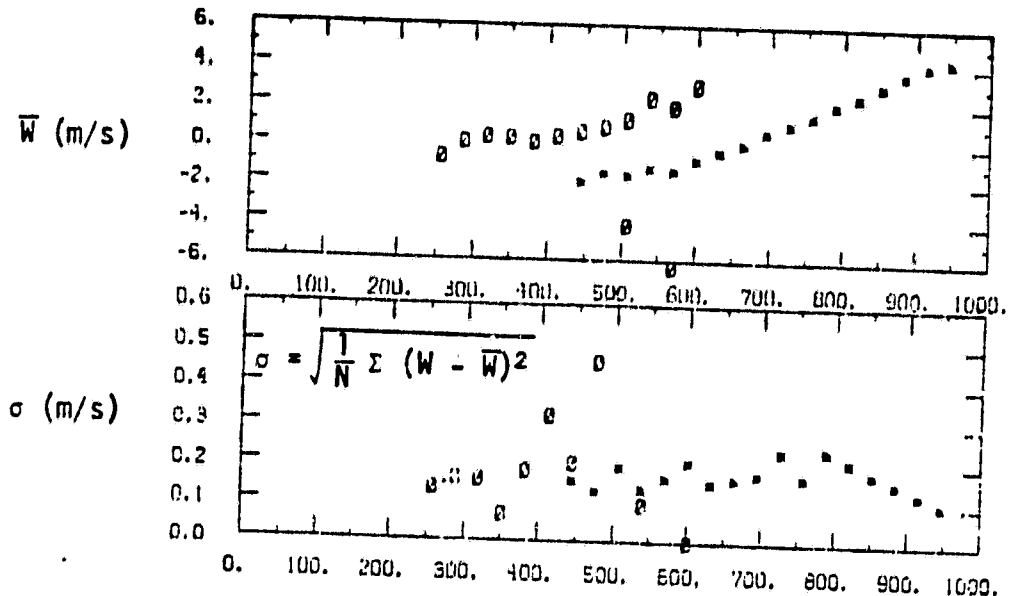
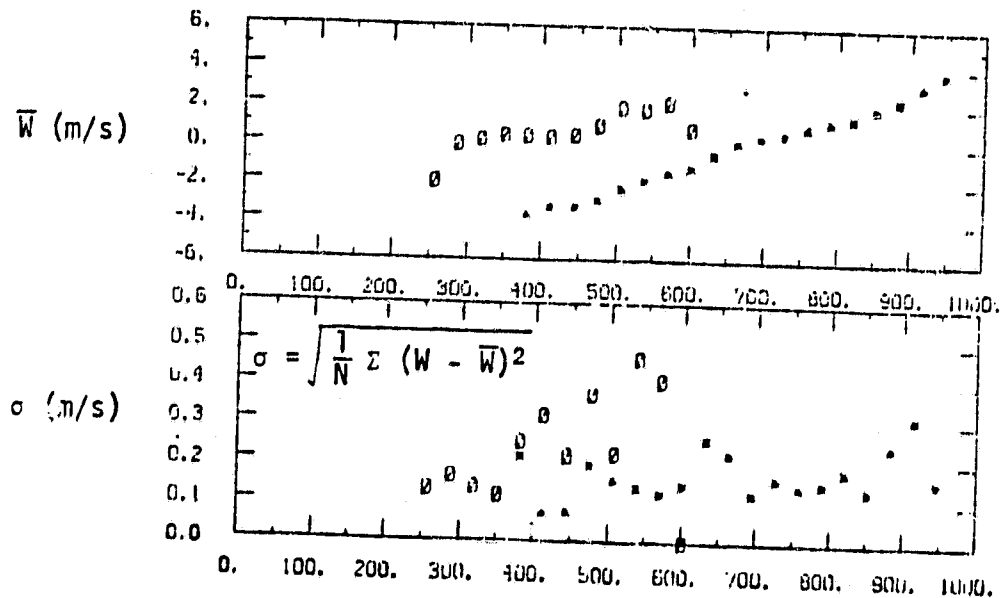


Figure 14 (cont'd).

ORIGINAL PAGE IS
OF POOR QUALITY



Run #7



Run #8

Figure 14 (cont'd.).

ORIGINAL PAGE IS
OF POOR QUALITY

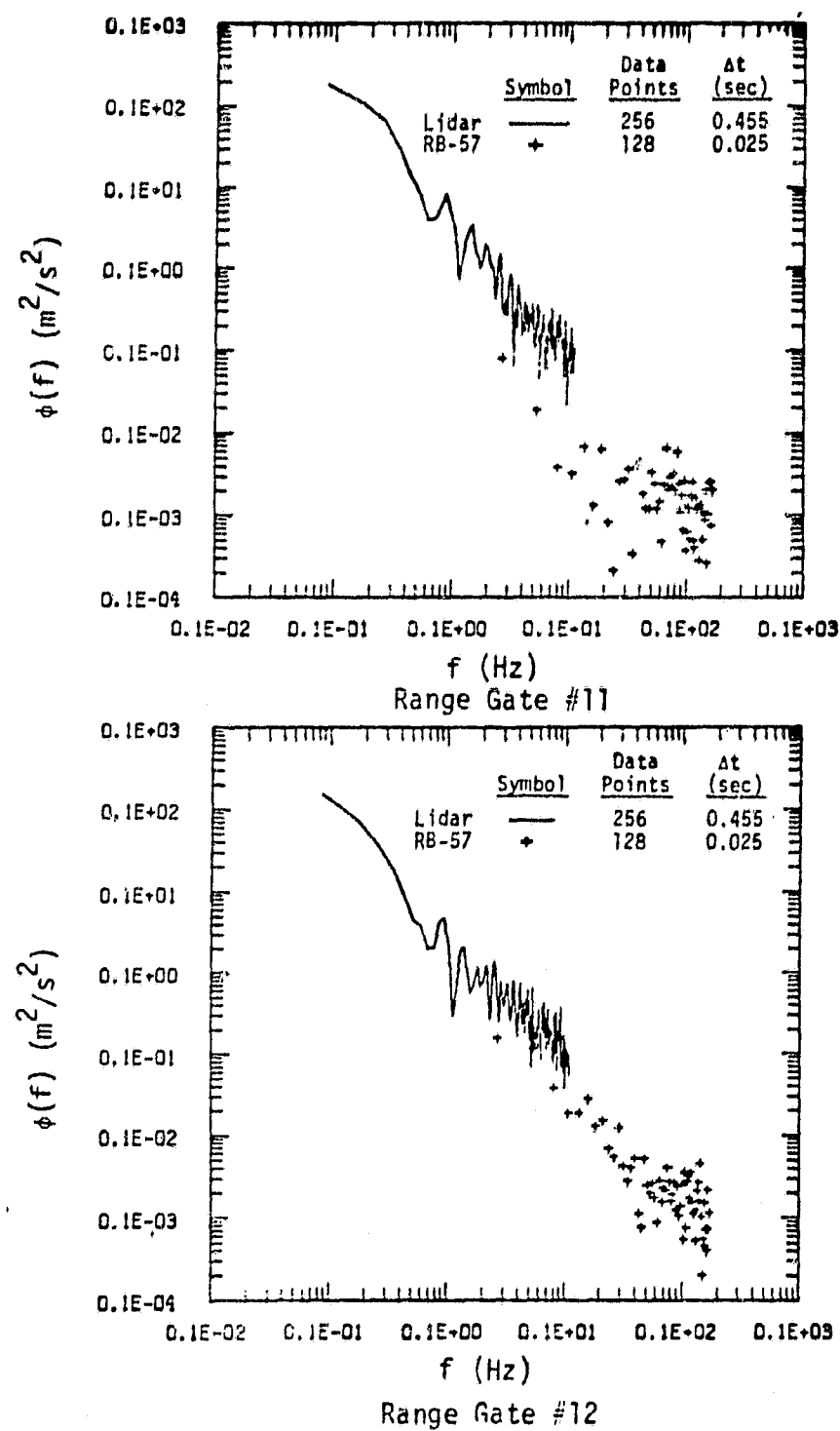


Figure 15 Radial velocity spectra.

ORIGINAL PAGE IS
OF POOR QUALITY

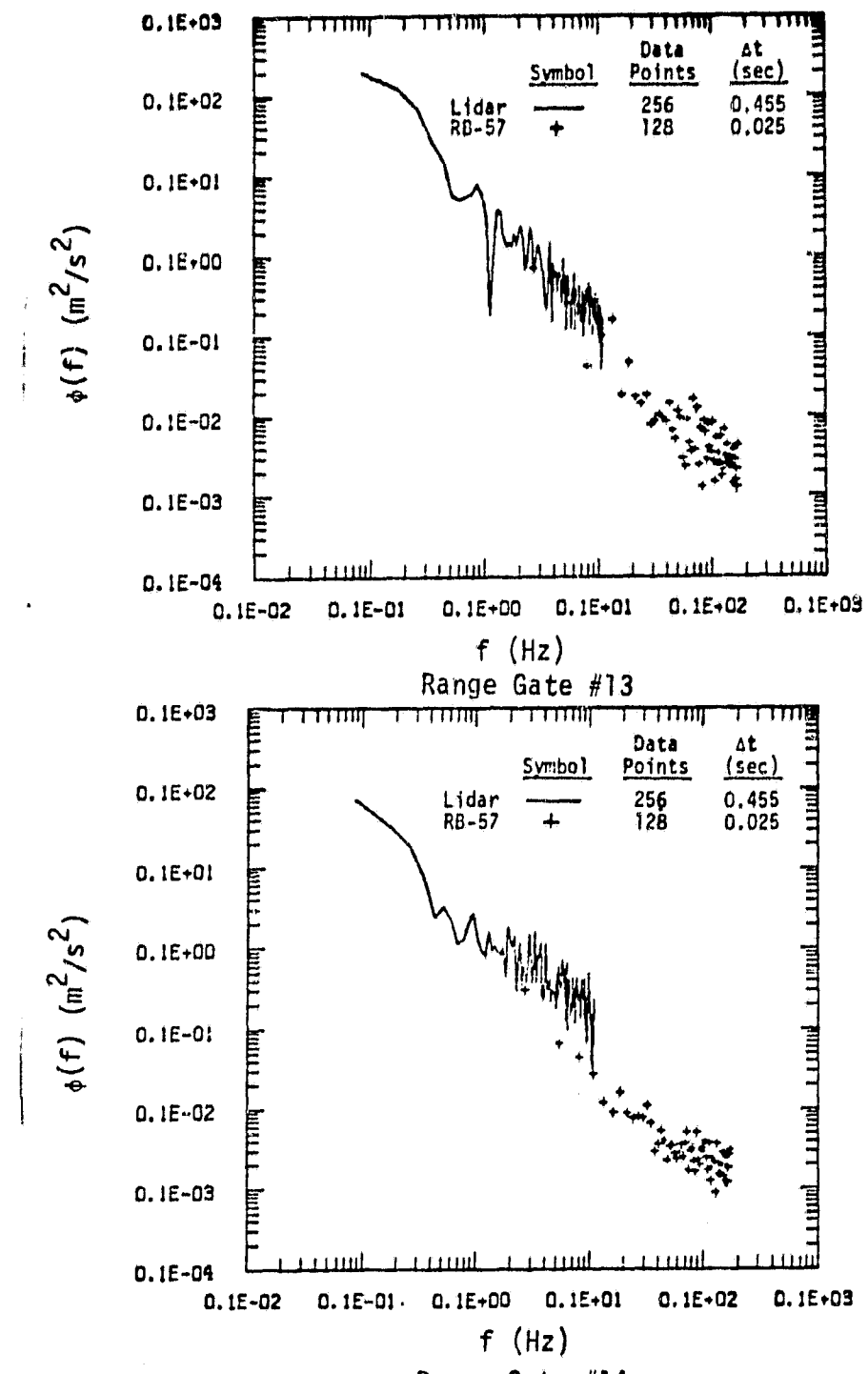


Figure 15 (cont'd.).

ORIGINAL PAGE 19
OF POOR QUALITY

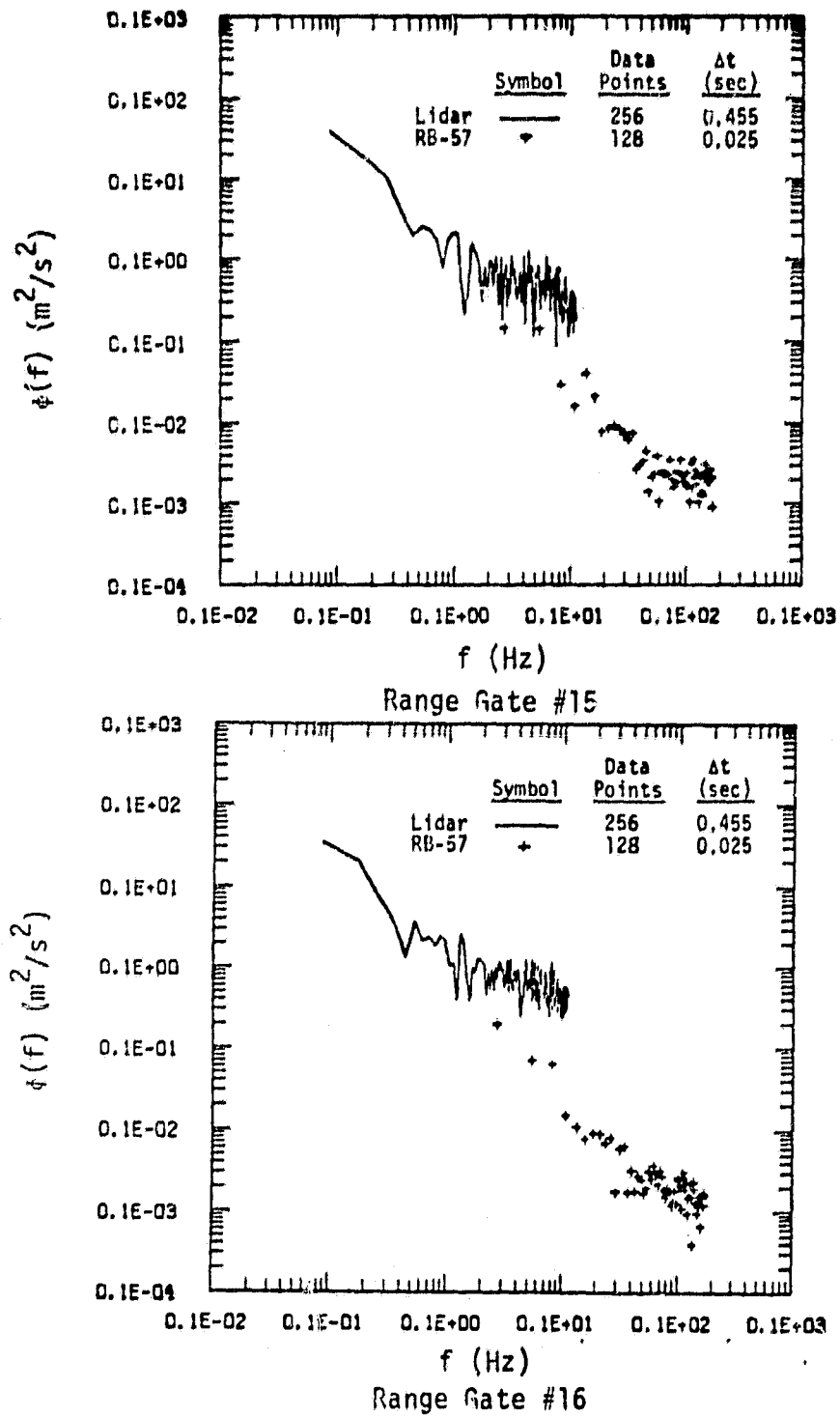


Figure 15 (cont'd.).

ORIGINAL PAGE IS
OF POOR QUALITY

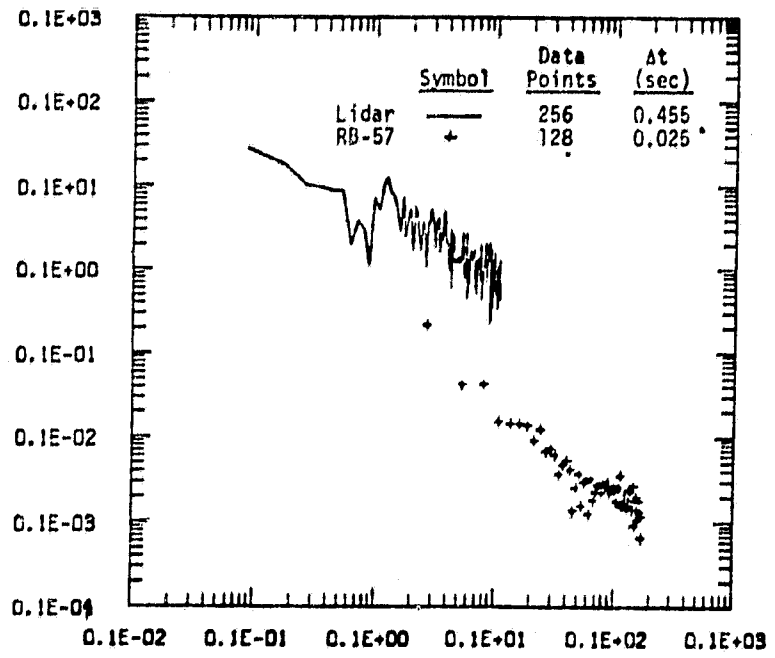
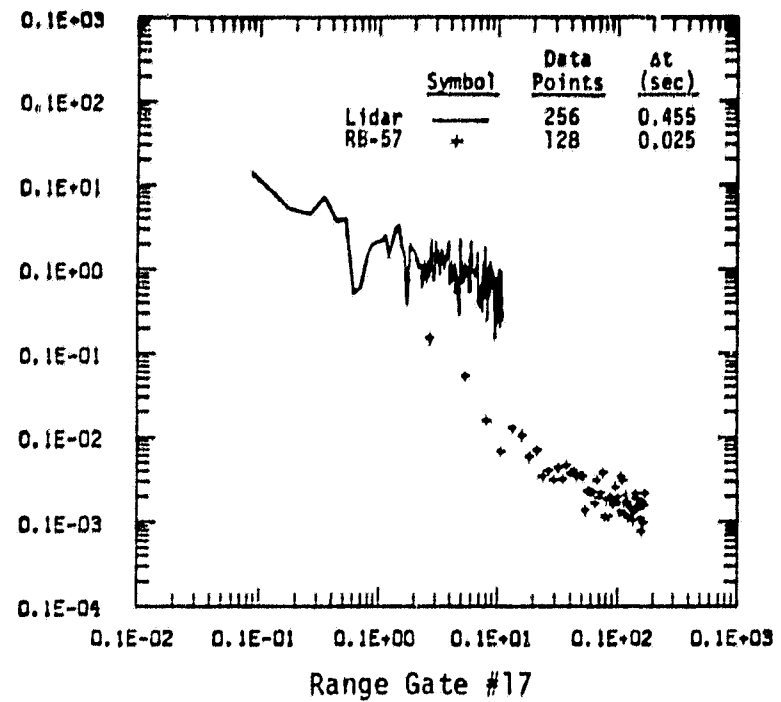


Figure 15 (cont'd.).

TABLE 1. VADS Tape Format (ground-based lidar).
(Format repeats every 0.455 seconds)

Word No.	Description	Format	LSB	Comment
1	Elevation	Integer	1	Degrees
2	Pitch	Integer	1	Degrees
3	Azimuth	Integer	1	Degrees
4	Minutes	Integer	1	Degrees
5	Seconds	Integer	10	Seconds
6	Status	Integer	Coded	See text
7	Pulse Width Code	Integer	Coded	See text
8	No. Pulses/Integration	Integer	1	
9	No. Lags	Integer	1	
10	Year	Integer	1	Date Collected
11	Month	Integer	1	Date Collected
12	Day	Integer	1	Date Collected
13	Run Number	Integer	1	
14	Record Number	Integer	1	0-32767
	Lidar Variables (3 values/range gate)			
15	Amplitude (intensity)	Integer	.184 dB	
16	Velocity	Integer	.08 m/s	
17	Width (variation) (M2)	Integer	.397 [10** (M2/10)]	
18-77	Additional groups of three variables for each range gate. The number of gates depends upon the pulse width.			

ORIGINAL PAGE IS
OF POOR QUALITY

TABLE 2. Values of Turbulence Intensity Versus Integer Index.

Integer Index	0	1	2	3	4	5	6	7	8
Lidar Width (m/s)	0.5	0.5	0.63	0.79	0.99	1.26	1.58	1.99	2.51
	9	10	11	12	13	14	15		
	3.15	3.97	5.0	6.29	7.92	9.98	12.56		

ORIGINAL PAGE IS
OF POOR QUALITY

TABLE 3. Sample of Aircraft Data.
Format 60-bit integer; Data sampled at 40/sec
Time increment = 0.025 sec

Channel	Units	Low	High	Mean	RMS	STD	Points
1 TIME	SFCNDRY	60245.518	60155.619	60200.56959	60200.57410	-25.96365	-3597.
2 PHI DOT	RAD/SEC	.019	-.096	.00365	.01062	.00997	-3597.
3 ACCL X CG	G UNITS	1.090	.863	.99918	.99918	.03021	3597.
4 THETA DOT	RAD/SEC	.027	-.029	.00421	.00833	.00718	-3597.
5 PHI	RAD	.104	-.011	.05904	.06506	.02506	-3597.
6 PSI 1	RAD	.233	.029	.009	.00095	.01457	.01405
7 DEL PSI 1	RAD	-.083	-.2474	-.230.202	-.231.53700	-.231.53770	-.53791
8 PSI 2	RAD	.592.400	.589.584	.590.87076	.590.87101	.54570	3597.
9 DEL PSI 2	RAD	.492	-.096	.97810	1.12784	.56162	3597.
10 ACCL X LT	G UNITS	1.197	.890	1.05113	1.05108	.93970	3597.
11 ACCL X RT	G UNITS	1.180	.858	1.01275	1.01366	.04300	3597.
12 ACCL X CG	G UNITS	.102	.018	.05903	.06197	.01884	3597.
13 ACCL Y CG	G UNITS	.116	-.119	-.02825	-.03230	-.03218	3597.
14 ALPHA CTR	RAD	.089	.042	.06642	.06694	.00843	3597.
15 BETA CTR	RAD	-.014	-.050	-.03430	-.03491	.00655	3597.
16 TEMP 1	DEG F	100.603	100.063	190.93517	100.43625	123.55	3597.
17 ACCL Z INS	G UNITS	1.118	.75.264	75.26517	75.26517	.01217	3597.
18 ALPHA RT	RAD	.133	.895	1.06573	1.00622	-.03136	3597.
19 BETA RT	RAD	-.023	-.011	.00567	.00822	.00594	3597.
20 ALPHA LT	RAD	.143	-.091	.11966	.12005	.02971	3597.
21 BETA LT	RAD	-.035	-.073	-.05295	-.05328	.00573	3597.
22 PSI DOT	RAD/SEC	.012	-.028	.00231	.00429	.00362	3597.
23 TEMP TOT	DEG C	23.613	19.675	21.60561	21.62879	1.00133	3597.
24 QC LT	PSID	.494	.416	.46167	.46213	.02066	3597.
25 QC CTR	PSID	.475	.398	.44336	.44353	.02937	3597.
26 QC RT	PSID	.511	.426	.47291	.47338	.02120	3597.
27 PS	PSIA	13.088	13.072	13.52465	13.52667	.22162	3597.
28 TEMP INT	VOLTS	2.31	1.058	.67738	.67743	.00259	3597.
29 HYGROM	DEG C	17.418	13.117	15.14038	15.17570	1.03933	3597.
30 QC2 LT	PSID	.010	-.008	.00913	.00126	.00126	3597.
31 QC2 CTR	PSID	.006	-.008	-.00000	.00110	.00110	3597.
32 QC2 RT	PSID	.011	-.010	.00013	.00135	.00135	3597.
33 DAR	DEG	2.300	-.994	1.03629	1.67183	.34051	3597.
34 DAL	DEG	2.314	-.992	-.23616	.42804	.37042	3597.
35 DELEV	DEG	1.094	-.017	.13313	.28073	.26719	3597.
36 DSTAB	DEG	-.859	-.1113	-.1.00993	1.01255	.07202	3597.
37 DRUD	DEG	1.693	.270	.61179	.63947	.19613	3597.
38 DT-MR	PCT MAX	.52.539	.31.641	.41.17247	.41.09654	.7.70240	3597.
39 DT-FL	PCT MAX	.48.730	.28.905	.37.6686	.38.39608	.7.54910	3597.
40 DFLP	POSITION	1.000	.996	.99965	.99965	.0105	3597.
41 DSY	POSITION	.936	.896	.90108	.90108	.00152	3597.
42 D10 G	METERS	9710859.725	99999.900	99999.900	99999.900	1.555	1.6007
43 S10 D	DEGREES	91.964	-.91.928	-.91.94570	-.91.94570	.01045	3597.
44 LONG	DEGREES	-.90.596	-.86.657	-.86.62664	-.86.62665	.01746	3597.
45 LAT	DEGREES	34.697	34.662	34.67005	34.67005	.01016	3597.
46 TPK ANG	DEGREES	235.878	234.079	234.99833	234.99833	.47691	3597.

ORIGINAL PAGE IS
OF POOR QUALITY

TABLE 3. (cont'd).

Channel	Units	High	Low	Mean	RMS	STD	Points
μ 2 HNG	RADIAN S	4.666	4.020	4.04005	4.04006	0.01005	3597.
μ 4 VE	M/SEC	-60.788	-62.844	-61.62267	61.62550	.59146	3597.
μ 5 VH	M/SEC	-61.497	-64.011	-63.12199	63.12997	.82327	3597.
μ 3 ALTITUDE	KM	.966	.475	.69945	.70916	1.13628	3597.
μ 4 DEGREES C		21.029	16.809	18.9001	18.93359	1.12733	3597.
μ 5 WND SPD KNOTS		1.006	-10.753	-4.71724	5.53695	2.89964	3597.
μ 6 WND SPD KNOTS		4.262	-3.091	1.51541	2.03614	1.36011	3597.
μ 7 WIND SPEED KNOTS		10.884	3.028	5.48462	5.89947	2.17297	3597.
μ 8 WIND DIREC DEGREES		195.937	65.357	117.12963	120.56660	28.58640	3597.
μ 9 AIRSPEED R	M/SEC	79.589	71.779	76.09744	76.11063	2.13561	3597.
μ 10 AIRSPEED C	M/SEC	76.766	69.404	73.70164	73.73120	2.07977	3597.
μ 11 AIRSPEED L	M/SEC	78.323	70.950	75.19102	75.21973	2.07944	3597.
μ 12 DELTA ALT METERS		0.000	-489.780	-268.47985	301.03519	116.28193	3597.
μ 13 HGT DISP METERS		0.000	-489.645	-268.66101	301.51089	136.87689	3597.
μ 14 WGT	M/SEC	3.529	-3.453	.00000	1.55347	1.55369	3597.
μ 15 CENTER	M/SEC	3.450	-3.075	.00000	1.54458	1.54479	3597.
μ 16 LEFT	M/SEC	3.533	-2.995	.00000	1.53227	1.53249	3597.
μ 17 VG RIGHT	M/SEC	2.000	-1.166	.00201	.52165	.52572	3597.
μ 18 VG CENTER	M/SEC	2.002	-1.277	-.00446	.55436	.55440	3597.
μ 19 VG LEFT	M/SEC	1.875	-1.648	-.00252	.50809	.52816	3597.
μ 20 VG PIGHT	M/SEC	.970	-.765	.01077	.20272	.20040	3597.
μ 21 WG CENTER	M/SEC	.510	-.859	.03223	.21630	.20945	3597.
μ 22 WG LEFT	M/SEC	.528	-1.067	.03050	.21167	.20969	3597.
μ 23 VESTHPSI	M/SEC	.956	-.653	.00900	.46257	.46274	3597.
μ 24 V10C0SPSI	M/SEC	.554	-1.012	.00900	.51661	.51649	3597.
μ 25 LYAPSPDNT	M/SEC	.007	-.094	.00000	.03389	.03383	3597.
μ 26 VRH	M/SEC	3.499	-4.310	.00000	2.10632	2.10661	3597.
μ 27 VCH	M/SEC	3.064	-4.297	.00000	2.08738	2.08767	3597.
μ 28 LYAPSPDNT	M/SEC	.091	-.098	.00000	.03517	.03517	3597.
μ 29 VLH	M/SEC	3.122	-4.241	.00000	2.07815	2.07844	3597.
μ 30 VRAETAR	M/SEC	1.307	-1.192	.00000	.44460	.44466	3597.
μ 31 VPSI	M/SEC	2.016	-1.541	.00051	.76535	.76544	3597.
μ 32 VECUSPSI	M/SEC	.761	-.520	.00000	.36032	.36837	3597.
μ 33 VHSINPSI	M/SEC	.696	-1.272	.00000	.64870	.64879	3597.
μ 34 LYAPSPDNT	M/SEC	.026	-.024	.00000	.00920	.00920	3597.
μ 35 VRALPHRPHI	M/SEC	.054	-.022	.00075	.01011	.00973	3597.
μ 36 VCBETAC	M/SEC	1.448	-.052	.00000	.47404	.47410	3597.
μ 37 VCP5I	M/SEC	1.954	-.1.493	.00528	.74150	.74158	3597.
μ 38 LYAPSPDNT	M/SEC	.448	-.052	.00000	.01875	.01975	3597.
μ 39 VCP5I	M/SEC	.040	-.050	.00157	.00911	.00897	3597.
μ 40 VCP5I	M/SEC	1.343	-.1.422	.00005	.43798	.43804	3597.
μ 41 VCP5I	M/SEC	1.991	-.1.523	.00490	.75626	.75635	3597.
μ 42 VCP5I	M/SEC	.026	-.024	.00000	.00920	.00920	3597.
μ 43 VLA1PHI	M/SEC	.642	-.121	.00160	.01252	.01241	3597.
μ 44 VRALPHAR	M/SEC	2.185	-.2.273	.01639	.73074	.73065	3597.
μ 45 VPHETA	M/SEC	3.192	-.834	-.04496	1.89853	1.89827	3597.